

2016

# Analysis of Photonic Integrated Circuits for Optical Coherence Tomography Application

Liangyue Yan  
*Lehigh University*

Follow this and additional works at: <http://preserve.lehigh.edu/etd>



Part of the [Electrical and Computer Engineering Commons](#)

---

## Recommended Citation

Yan, Liangyue, "Analysis of Photonic Integrated Circuits for Optical Coherence Tomography Application" (2016). *Theses and Dissertations*. 2893.

<http://preserve.lehigh.edu/etd/2893>

This Thesis is brought to you for free and open access by Lehigh Preserve. It has been accepted for inclusion in Theses and Dissertations by an authorized administrator of Lehigh Preserve. For more information, please contact [preserve@lehigh.edu](mailto:preserve@lehigh.edu).

**Analysis of Photonic Integrated Circuits for Optical Coherence  
Tomography Application**

By  
Liangyue Yan

A Thesis  
Presented to the Graduate and Research Committee  
of Lehigh University  
in Candidacy for the Degree of  
Master of Science

in  
Electrical and Computer Engineering

Lehigh University  
September 2016

This thesis is accepted and approved in partial fulfillment of the requirements for the Master of Science.

Date: August 3<sup>rd</sup> 2016

---

Prof. Nelson Tansu, MS Advisor

---

Prof. Doug R. Frey, Assoc. ECE Chair

## **Acknowledgement**

The completion of this thesis could not be possible without the guidance and encouragement of so many people. It is a great pleasure to study and work under the guidance of Prof. Nelson Tansu, who are always filled with his boundless knowledge, his strong work motivation, and his great passion for guiding and encouraging students to continuously getting better. I will not get this much improvement without such an adorable advisor and mentor for my master's study. I would like to express my sincere gratitude to our seniors: Dr. Chee Keong Tan (now Prof. Chee-Keong Tan), and Mr. Wei Sun for tremendous help they offered; Such assistance, guidance and suggestion are precious and irreplaceable, and have contributed immensely to the completion of the thesis. In addition, I also owe a deep gratitude to Prof. Chao Zhou of whom our group has collaborated on this topic discussed in this thesis.

On a personal note, I would like to express my thanks to my peers: Yiming Zhong, Damir Borovac, and Ioannis Fragkos. On personal note, I would also like to thank Chong Shen and Yiming Zhong for their encouragement and support. Last but not least, I am extremely thankful to my parents 颜传法 and 王丽春 for raising me, supporting me, and encouraging me till today.

# Table of Contents

Acknowledgement .....	iii
List of figure .....	v
Abstract .....	1
1. Introduction.....	2
1.1. Background and motivation .....	2
1.1.1.Optical coherence tomography and photonic integrated circuits.....	2
1.1.2.Motivation.....	4
1.2. Thesis organization .....	5
References for chapter 1 .....	6
2. Theory of Loss Analysis in PIC design .....	7
2.1. Surface roughness loss .....	7
2.2. Waveguide bending loss .....	12
2.3. Tapered Waveguide .....	15
2.4. Coupler structure.....	19
2.5. Intersection crosstalk .....	24
References for chapter 2 .....	29
3. Numerical simulation on loss analysis and optimization.....	30
3.1. Introduction of Finite-Difference-Time-Domain (FDTD) method.....	30
3.2. Surface roughness .....	32
3.3. Bend design.....	34
3.4. Tapered waveguide design and simulation results.....	38
3.5. Coupler simulation.....	41
3.6. Waveguide intersection analysis.....	45
3.7. Total optimized loss for PIC-based OCT.....	49
References for chapter 3 .....	52
4. Summary and future direction .....	54
4.1. Conclusion .....	54
Curriculum Vitae.....	56

## List of figure

Figure 1-1. Schematic diagram of OCT system [6].....	3
Figure 1-2. Schematic diagram interferometer of PIC board connecting with laser source [1]. ....	4
Figure 2-1. Two Dimensional model for waveguide with rough interface. $2a$ is average width, $n_2$ and $n_1$ represent core and cladding refractive index respectively. And the incident TE mode has a propagation constant $\beta$ .....	8
Figure 2-2. Scattering loss as a function of waveguide width $2a$ for roughness $\sigma=3\text{nm}$ at $\lambda=1310\text{nm}$ and $\lambda=1550\text{nm}$ . ....	11
Figure 2-3. Scattering loss versus waveguide width, compare results between $\sigma = 3\text{nm}$ , $\sigma = 5\text{nm}$ and $\sigma = 8\text{nm}$ , and wavelength is $\lambda = 1310\text{nm}$ . Vertical labels are logarithm.....	12
Figure 2-4. Geometry of waveguide bend with coordinate $x$ [8].....	13
Figure 2-5. Calculated results of bending loss with respect to the bending radius $R$ , where the wavelength = $1310\text{nm}$ , and waveguide width is $4\mu\text{m}$ . ....	14
Figure 2-6. Configuration of a ragular lateral tapered waveguide [15]. ....	15
Figure 2-7. Slowing varying waveguide [16]. ....	16
Figure 2-8. Transmittance versus taper length, where the taper strucutre is silicon on top of silica, with $TE_0$ , $\lambda = 1.31\mu\text{m}$ , and $2a_1 = 9.5\mu\text{m}$ , $2a_0 = 4\mu\text{m}$ .....	19
Figure 2-9. Schematic diagram of the coordinate axes for the analysis of parallel waveguides. $2a$ is waveguide width in $y$ direction, $S$ is spacing between two waveguides, $2d$ is distance between centers of two parallel waveguides. Put coordinate axes at center of waveguide #1. ....	20
Figure 2-10. Figure (a) shows logarithm plot of coupling coefficient as function of waveguide spacing $S$ , when waveguide width @ $2a = 4\mu\text{m}$ . Figure (b) shows logarithm plot of coupling	

coefficient as function of waveguide width, when spacing between two waveguides is  $S=0.2 \mu\text{m}$ . Both results is @  $\lambda = 1.31 \mu\text{m}$ ..... 22

Figure 2-11 (a): Power distribution of two waveguides varies along propagating direction. (b): logarithm plot of complete coupling length as function of waveguide spacing, @ $\lambda = 1.31\mu\text{m}$  and  $\lambda = 1.55 \mu\text{m}$ , where waveguide width is  $2a = 4\mu\text{m}$ , and coupling length is in unit of mm..... 23

Figure 2-12. Schematic diagram of coordinate axes for analysis of intersecting waveguides. ... 24

Figure 2-13 Eigenvalue of TE mode, even mode have relation of  $\tan U = WU$ , and odd mode have relation function:  $\tan U = -U/W$ , and the black spots denote parameter U for a specific waveguide structure[14]..... 26

Figure 2-14 Coupling coefficient as function of core width  $2a [\mu\text{m}]$  for crossing angles at 15, 18 and 20 degree, respectively. The waveguide structure has silicon core with  $n_2=3.5$ , and silica cladding layer with  $n_1=1.5$  with operating wavelength  $\lambda = 1.31\mu\text{m}$ . ..... 27

Figure 2-15. Crosstalk power in dB from waveguide #1 to waveguide #2 as function of intersection angle, where  $a=2\mu\text{m}$ ,  $\lambda = 1.31\mu\text{m}$ . ..... 28

Figure 3-1. Schematic of Yee's 1-D EM field with space and time reference[2]. ..... 31

Figure 3-2. Three-dimensional of Yee's EM field cell[3]. ..... 31

Figure 3-3. X and Y matrix containing n by m elements representing discrete in real space[11].33

Figure 3-4. Calculated scattering loss as a function of waveguide width ( $\mu\text{m}$ ), with waveguide height= $4.5 \mu\text{m}$ ,  $\lambda = 1.31\mu\text{m}$ , correlation length  $L_c = 20\text{nm}$ . The plot is in logarithmic scale. . 34

Figure 3-5. Schematic of waveguide bend in SOI [12]. ..... 35

Figure 3-6. Transmittance of 90-degree waveguide bending versus curvature radius ( $\mu\text{m}$ ), the waveguide dimension is width at  $4\mu\text{m}$  and height of  $4.5\mu\text{m}$ . A comparably low radiation loss can be achieved at radius =  $2000 \mu\text{m}$ . ..... 35

Figure 3-7. Comparison of waveguide bending, (a) is top view of bending without lateral offset; (b) is top view of bending with lateral offset [4]. ..... 36

Figure 3-8. Ex component of fundamental TE mode for silicon ridge waveguide having height of  $4.5 \mu\text{m}$ , and width of  $4 \mu\text{m}$  for different bent radius. (a) Radius =  $100 \mu\text{m}$ , (b) Radius =  $500 \mu\text{m}$ , (c) Radius =  $1000 \mu\text{m}$ , (d) Radius =  $5000 \mu\text{m}$ . ..... 37

Figure 3-9. Bending loss of waveguide as a function of lateral offset ( $\mu\text{m}$ ) with lowest loss at lateral offset= $0.12 \mu\text{m}$ . ..... 37

Figure 3-10. (a) tapered waveguide structure connecting with two waveguides with different width, red portion represents for silicon waveguide, and gray portion is silicon-dioxide substrate. (b) FDTD simulation results for a linearly tapered waveguide, where tapering length is  $66 \mu\text{m}$ , input waveguide width is  $9.5 \mu\text{m}$ , and output waveguide width is  $4 \mu\text{m}$ . Fundamental mode is initiated inside input waveguide. .... 38

Figure 3-11. Simulation results show power transmission in tapered waveguide as function of tapering shape parameter  $m$ . the tapered waveguide connects two waveguides, where the input waveguide width is  $9.5 \mu\text{m}$ , output waveguide width is  $4 \mu\text{m}$ , waveguide height is  $4.5 \mu\text{m}$ , tapering length is  $60 \mu\text{m}$ , and operating wavelength is  $\lambda = 1.31 \mu\text{m}$ . ..... 41

Figure 3-12. Simulation results of taper loss versus tapering length  $L$  at taper shape parameter  $m=1.5$  comparing with  $m=1$ (linear tapering). ..... 41

Figure 3-13. (a) Schematic of waveguide coupler, where the bending section determine the proximity between two waveguides. (b) Coupler cross-section in Lumerical FDTD solutions, where silicon waveguides are placed on top of silicon-dioxide substrate with air gap between two waveguides. .... 42



Figure 3-14. FDTD simulation for  $TE_{10}$  mode with  $h=4.5\mu m$ ,  $w=4\mu m$ ,  $\lambda = 1.31\mu m$ . Figure (a) shows the guided mode; figure (b) shows the evanescent mode; figure (c) shows a clearer view of evanescent field in between two waveguides. .... 44

Figure 3-15. Eigen mode in symmetric directional coupler: (a) shows the guided mode and (b) shows the evanescent mode. .... 44

Figure 3-16. Power coupling between two waveguides back and forth, where coupler structure is  $w=0.5\mu m$ ,  $h=0.2\mu m$ ,  $s=50\text{ nm}$ , and  $\lambda = 1.55\mu m$ . Coupling length for this coupler structure is  $12.887\mu m$  [23]. .... 44

Figure 3-17. Coupling length versus coupler spacing for SOI ridge 50/50 directional coupler with fundamental mode, the waveguides have height of  $h=4.5\mu m$ , width of  $w=4\mu m$ , and the operating wavelength is  $\lambda=1.31\mu m$ . .... 45

Figure 3-18. Schematic of waveguide intersection. Figure (a) is the schematic of directional intersecting waveguide with crossing region being defined. Figure (b) represents the structure of low-loss and low-crosstalk waveguide intersection we proposed, ellipse at each arm of intersection have long radius  $a$  and short radius  $b$ ,  $x$  is offset between ellipse and center point of crossing region. .... 46

Figure 3-19. FDTD simulation picture of waveguide intersection with  $b=4\mu m$ . Figure (a) shows proposed crossing with  $a=10\mu m$ ,  $x= 0\mu m$ . Figure (b) shows proposed crossing with  $a=10\mu m$ ,  $x=1.4\mu m$ . Figure (c) shows proposed crossing with  $a=9\mu m$ ,  $x=0.7\mu m$ . figure (d) shows proposed crossing with  $a=10.2\mu m$  ,  $x=0.7\mu m$ . .... 48

Figure 3-20. Simulation results of transmission loss as function of lateral shift and long radius. Figure (a) shows transmission loss versus lateral shift  $x$  for proposed intersection structure with

a=10  $\mu m$  and b=4  $\mu m$ ; figure (b) shows transmission loss versus long radius a, simulated intersecting structure has b=4  $\mu m$  and x=0.7  $\mu m$ . ..... 49

Figure 3-21. PIC layout with tapered waveguide [29]..... 50

## **Abstract**

Nowadays, optical coherence tomography (OCT) technology is well known in the in-vivo disease diagnose, attributed to the low-cost operation of the three-dimensional medical imaging. In this thesis, we investigate the potential of using photonic integrated circuits (PIC) technologies for replacing the free space optical components in the OCT. The use of Silicon-photonics CMOS based technologies are employed in investigating the building blocks of the PIC used for enabling replacement of free-space optics interferometer part in OCT system. The building block of the structures include the roughness consideration, tapered waveguides structures, bend loss analysis, coupler analysis, and cross talk in intersecting waveguides. The technologies platform was developed based on Silicon-on-Insulator (SOI) technologies. Future directions of the concept are also presented in this thesis.

# 1. Introduction

## 1.1. Background and motivation

Optical coherence tomography (OCT) is a non-invasive and low-cost medical imaging method with the capability of creating micro-scale three-dimensional images for human body tissue [1-2]. Currently the OCT system mainly consists of several free space optical components leading to the bulky size of the instrument. However, a compact size portable OCT system can be achieved by replacing the conventional free space optical components in OCT system with the photonic integrated circuit (PIC). Note that in a PIC based OCT system, achieving low-loss silicon-on-insulator (SOI) PIC board is critical to acquiring high-resolution images for medical usage. This thesis aims at developing a method of accessing low-loss PIC board for the potential OCT applications. The key sources of the loss in a OCT-PIC board is described and analyzed both analytically and numerically.

### 1.1.1. Optical coherence tomography and photonic integrated circuits

Optical coherence tomography (OCT) is one of the approaches for optical tomography which have been developed since 1980s [3]. Benefiting from the high penetration depth and transversal resolution, the OCT has been widely applied as the safe, cheap, and non-invasive technique in medical field for disease diagnosis, such as ophthalmology, cardiology and dermatology [4]. Generally, the OCT synthesizes the cross-sectional images by performing the low coherence interference between the depth-scan beam reflected from tissue samples and the beam from reference sample [5]. Afterwards, the Fourier transformation will be carried out to create tissue profile in the depth dimension. Figure 1-1 shows the schematic diagram of an OCT system [6], where the major part of the interferometer and optical scanning and probing are formed by the optical fibers and free space optical components with a bulky geometry size . In order to

achieve higher stability and efficiency in a compact size, such fragile fibers and free space optical components can be integrated and replaced by the PIC components. In this case, a novel OCT system with the merit of low-cost, small dimension, and portability can be obtained.

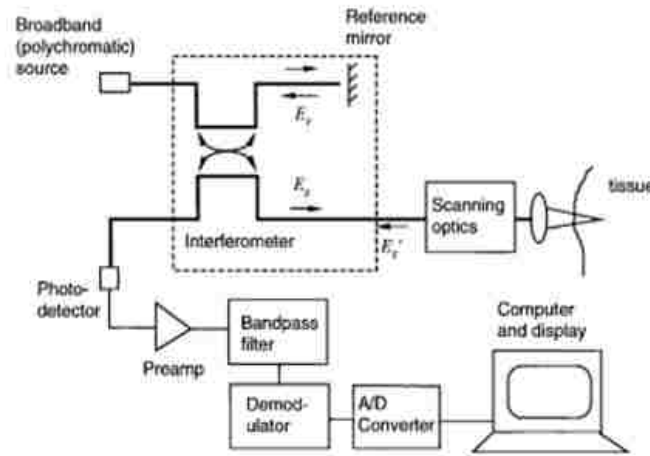


Figure 1-1. Schematic diagram of OCT system [6].

Photonic integrated circuits (PICs) are similar to electronic integrated circuits (EICs) but with various functions for optical applications. PICs can be fabricated through same process as the EICs with lithography and multiple etching steps [2]. In the typical PICs, optical waveguide is one of the fundamental elements meaning that all other components are modified from the waveguide. PICs can be fabricated based on many different materials. For example, GaAs and InP can be incorporated as the high efficiency light source in PICs [7];  $Si_3N_4$  based PICs yield transparency in visible and infrared spectrum regime with high-index-contrast [8]; silica PICs come with the characteristics of low-loss and thermal stability [9]; and silicon PICs with high-index-contrast can be easily manufactured through the CMOS fabrication method [2, 10].

### 1.1.2. Motivation

Silicon photonics is a low-cost multi-functional platform for integrated photonic applications. Because of the maturity of CMOS industry, silicon photonics with various optical functions can be easily manufactured and integrated via cost efficient and micro-scale fabrication process. Furthermore, the high-index-contrast in silicon PICs yields the high optical confinement, which enables compact photonic devices. In that case, a compact interferometer design for OCT system can be achieved with silicon PICs. In an interferometer for OCT system, interference happens between two different light signals that reflected from tissue sample and reference arm respectively. Both of these two light signals should propagate the same optical length.

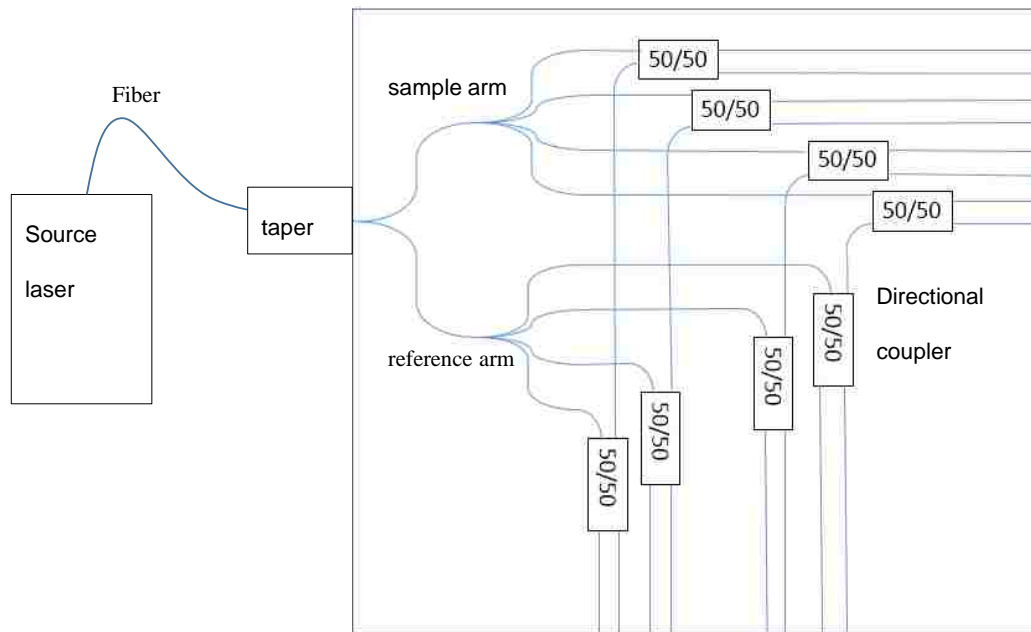


Figure 1-2. Schematic diagram interferometer of PIC board connecting with laser source [1].

Fig 1-2 shows the design of the interferometer in a PIC board for OCT applications [1]. The input signal is generated from a monolithic optical source and then coupled into an optical fiber. In order to couple the light signal into the PIC board, a tapered waveguide is used as the intermedia between the fiber and PIC board. Then, the input light signal is split into one sample

arm and one reference arm by the first optical splitter. Using one 1x4 optical splitter and four 50/50 directional couplers, the light signal in sample arm is split into eight lines to be projected on tissue sample. Afterwards, the reflected beams from the tissue sample are collected back into the waveguides, and are mixed with the reference signals at the 50/50 directional couplers in reference arm.

In this thesis, the PIC board are based on the silicon-on-insulator (SOI) structure, in which all the optical components are made by putting silicon wire on top of silicon-dioxide substrate. Reducing optical loss in the SOI based interferometer PIC board is crucial for obtaining high-resolution OCT image. In our case, the optical losses are mainly attributed to the surface roughness in SOI based waveguides, tapered waveguide structure, waveguide bends, directional coupler, and waveguide intersection in the PIC board. Thus, the analyses for optical losses in each optical component of the PIC board are discussed in the following chapters.

## 1.2. Thesis organization

Chapter 1 introduces the background and motivation of developing low loss PIC board for OCT applications. In our case, the loss source from PIC board can be divided into five categories: waveguide roughness, waveguide bends, tapered waveguide structure, waveguide intersection and waveguide coupler. Accordingly, our analyses are performed for each source respectively. In Chapter 2, all the five components are interoperated based on analytical models, and the transmission efficiency of each part is calculated. In Chapter 3, the numerical simulations are carried out for each component respectively through Finite-Difference Time-Domain (FDTD) method. The summary and future direction is presented in Chapter 4.

## References for chapter 1

1. Y.Y. Huang, W.S., L.Y. Yan, A.Nitkowski, A. Weinroth, N. Tansu, and C. Zhou, *Integrated Photonic Devices for Ultrahigh-Speed, Space-Division Multiplexing Optical Coherence Tomography*. 2016.
2. Yurtsever, G., et al., *Photonic integrated Mach-Zehnder interferometer with an on-chip reference arm for optical coherence tomography*. Biomedical optics express, 2014. **5**(4): p. 1050-1061.
3. Fercher, A.F., et al., *Optical coherence tomography-principles and applications*. Reports on progress in physics, 2003. **66**(2): p. 239.
4. Parekh, M., et al., *Aniridia: recent developments in scientific and clinical research*. 2015: Springer.
5. Huang, D., et al., *Optical coherence tomography*. Science (New York, NY), 1991. **254**(5035): p. 1178.
6. Schmitt, J.M., *Optical coherence tomography (OCT): a review*. IEEE Journal of selected topics in quantum electronics, 1999. **5**(4): p. 1205-1215.
7. Narasimha, A., et al. *A 40-Gb/s QSFP optoelectronic transceiver in a 0.13  $\mu\text{m}$  CMOS Silicon-on-Insulator Technology*. in *Optical Fiber Communication Conference*. 2008. Optical Society of America.
8. Zhuang, L. et al. *Low-loss, high-index-contrast  $\text{Si}_3\text{N}_4/\text{SiO}_2$  optical waveguides for optical delay lines in microwave photonics signal processing*. Opt. Express, 2011. **19**(23): p. 23162–23170.
9. Doerr, C.R. and K. Okamoto, *Advances in silica planar lightwave circuits*. Journal of Lightwave Technology, 2006. **24**(12): p. 4763-4789.
10. Mekis, A., et al., *A grating-coupler-enabled CMOS photonics platform*. IEEE Journal of Selected Topics in Quantum Electronics, 2011. **17**(3): p. 597-608.



## 2. Theory of Loss Analysis in PIC design

Photonic integrated circuits usually consist of various fundamental photonic building blocks or components including SOI based waveguides, tapered waveguide structure, waveguide bends, directional coupler, and waveguide intersection. PIC board with different functions for can be obtained by integrating different components in one system. However, when the light signal propagates through those components, optical loss will be introduced as a result of waveguide imperfection, reflection, power leakage, and crosstalk, etc. Those optical losses will affect the performance of the PIC system. Specifically, in our case the optical loss in the PIC system dramatically degrade the OCT image quality. In this chapter, five major optical losses and their mechanism are analyzed based on the analytical models.

### 2.1. Surface roughness loss

During the fabrication of silicon waveguide, the etching process will introduce the surface roughness to the sidewall of the waveguide. Therefore, scattering loss arises when optical rays hit the rough sidewall of the waveguide. During this process, part of the power is radiated outside of the waveguide. Similar to the optical grating, sidewall roughness can be treated as a special grating in which the waveguide width varies randomly [1]. When the propagating light is projected on the grating, it forms dipole on the sidewall [2]. The light from dipoles scatters in all directions, and thus scattering loss takes place. In this section, an analytical model developed by Payne and co-workers is reviewed to evaluate how the sidewall roughness affects the scattering loss [3]. Our calculations in this section follow the same treatment that proposed by Payne and co-workers in their paper [3].

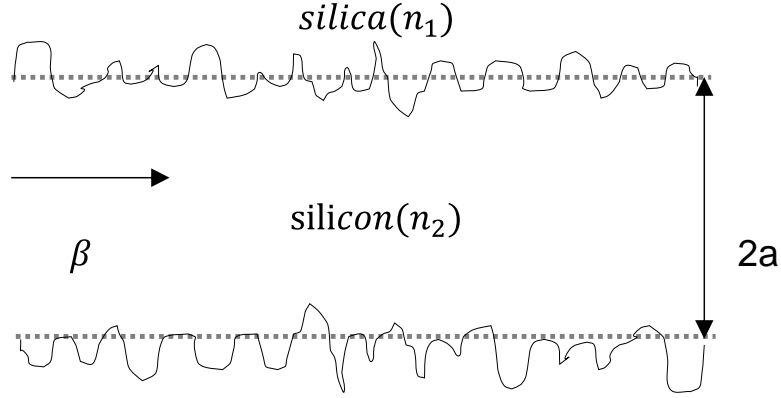


Figure 2-1. Two Dimensional model for waveguide with rough interface.  $2a$  is average width,  $n_2$  and  $n_1$  represent core and cladding refractive index respectively. And the incident TE mode has a propagation constant  $\beta$ .

Since sidewall roughness exists at only lateral surfaces of waveguide, a two dimensional silicon-on-silica waveguide model can be utilized to simplify the analysis. *Figure 2-1* shows the two dimensional silicon-on-silica waveguide model. In this model,  $2a$  represents the waveguide width while  $\beta$  is the propagation constant inside the waveguide. The refractive index of the silica and silicon are denoted as  $n_1$  and  $n_2$  respectively. Equation (2-1) represents the scattering loss model due to the surface roughness, where  $\varphi(a)^2$  is a modal field with waveguide geometrical parameters. The lateral surface roughness of the waveguide is described by the power spectra density function  $\tilde{R}(\Omega)$ , in which  $\Omega = \beta - n_1 k_0 \cos\theta$  is the scattering angle relative to waveguide axis. The propagation constant  $\beta = k_0 n_{eff}$  is determined by the effective index  $n_{eff}$  and the free space wavenumber  $k_0$ .

$$\alpha_{cm^{-1}} = \varphi(a)^2 (n_2^2 - n_1^2)^2 \frac{k_0^3}{4\pi n_2} \int_0^\pi \tilde{R}(\beta - n_1 k_0 \cos\theta) d\theta \quad (2-1)$$

Corresponding to treatment proposed by Payne and co-workers, the calculation of power spectra density function  $\tilde{R}(\Omega)$  can be linked to the autocorrelation function (ACF)  $R(u)$  shown in equation (2-2). Autocorrelation function  $R(u)$  is characterized by roughness mean square deviation

$\sigma^2$  from a flat surface, correlation length  $L_c$  and propagating distance  $u$ . According to literatures [3, 4], exponential autocorrelation function (ACF)  $R(u)$  is suitable to evaluate large waveguide roughness. In that case, the autocorrelation function can be written as equation (2-3).

$$\tilde{R}(\Omega) = \frac{1}{2\pi} \int_{-\infty}^{+\infty} R(u) \exp(i\Omega u) du \quad (2-2)$$

$$R(u) = \sigma^2 \exp\left(-\frac{|u|}{L_c}\right) \quad (2-3)$$

The integration of the spectra density function  $\tilde{R}(\Omega)$  can be denoted by  $S$ . This term can be treated as stated in literature [6]:

$$S = \int_0^\pi \int_{-\infty}^{+\infty} \sigma^2 \exp\left(-\frac{|u|}{L_c}\right) \exp(i(\beta - n_1 k_0 \cos\theta)u) du d\theta \quad (2-4)$$

and:

$$S = \sqrt{2}\sigma^2 L_c \pi \frac{\sqrt{\sqrt{4\beta^2 L_c^2 + [1 - L_c^2(\beta^2 - n_1^2 k_0^2)]^2} + 1 - L_c^2(\beta^2 - n_1^2 k_0^2)}}{\sqrt{4\beta^2 L_c^2 + [1 - L_c^2(\beta^2 - n_1^2 k_0^2)]^2}} \quad (2-5)$$

Eventually, scattering coefficient could be written as:

$$\alpha_{cm^{-1}} = \frac{\sigma^2}{\sqrt{2}k_0 a^4 n_1} g(V) f_e(x, y) \quad (2-6)$$

where  $g(v)$  and  $f(x, y)$  are complex functions defined with normalized waveguide parameters,  $U$ ,  $V$ ,  $W$  and dimensionless combination of  $\sigma$ ,  $a$  and  $L_c$  [6, 7].

$$U = a \sqrt{n_2^2 k_0^2 - \beta^2} \quad (2-7)$$

$$V = k_0 a \sqrt{n_2^2 - n_1^2} \quad (2-8)$$

$$W = a\sqrt{\beta^2 - n_1^2 k_0^2} \quad (2-9)$$

Note that  $g(v)$  is given as:

$$g(V) = \frac{V^2 v^2}{1+W} \quad (2-10)$$

Also, the modal field  $\varphi^2(d)$  at the equation (2-1) can be written as:

$$\varphi^2(a) = \frac{2V(1-b)}{a(V + \frac{1}{\sqrt{b}})} \quad (2-11)$$

Where  $b$  is normalized propagation constant:

$$b = \frac{\beta^2 - n_1^2 k_0^2}{(n_2^2 - n_1^2) k_0^2} \quad (2-12)$$

$f_e(x, y)$  is defined as :

$$f_e(x, y) = \frac{x\sqrt{(1+x^2)^2 + 2x^2 y^2 + 1 - x^2}}{\sqrt{(1+x^2)^2 + 2x^2 y^2}} \quad (2-13)$$

where parameter  $x$  represents a normalized correlation length, and  $y$  represents the normalized guiding coefficient. The expressions of these dimensionless parameters are given as:

$$\Delta = \frac{n_2^2 - n_1^2}{2n_2^2} \quad (2-14)$$

$$x = W \frac{L_c}{a} \quad (2-15)$$

$$y = \frac{n_1 V}{n_2 W \sqrt{\Delta}} \quad (2-16)$$

In a waveguide with strong optical confinement,  $y \approx 1$ , then equation (2-13) can be simplified as:

$$f_e(x, y) \approx \frac{x\sqrt{2}}{1+x} \quad (2-17)$$

The maximum result for  $f_e(x, y)$  is  $1/\sqrt{2}$  when  $x=1$ . Thus, the scattering loss coefficient is:

$$\alpha \leq \frac{\sigma^2}{\sqrt{2}k_0 a^4 n_1} g(V) \quad (2-18)$$

In unit of dB/cm, the scattering loss would be:

$$\alpha(\text{dB/cm}) = 4.34 \frac{\sigma^2}{\sqrt{2}k_0 a^4 n_1} g(v) \quad (2-19)$$

Figure 2-2 shows scattering loss with respect to the waveguide width at  $\lambda = 1310$  nm and  $\lambda = 1550$  nm respectively. In our calculation, a silicon-on-insulator (SOI) waveguide is used with core refractive index of 3.5 and cladding refractive index of 1.5. The surface roughness  $\sigma$  is set to 13nm. As shown in this figure, the scattering loss induced by surface roughness decreases exponentially as the waveguide width increases. Typically, when the waveguide width increases to 4  $\mu\text{m}$ , the scattering loss is  $\sim 0.26$  dB/cm for both wavelengths. Meanwhile, the scattering loss also depends on the light wavelength, where longer wavelength yields slightly higher scattering loss.

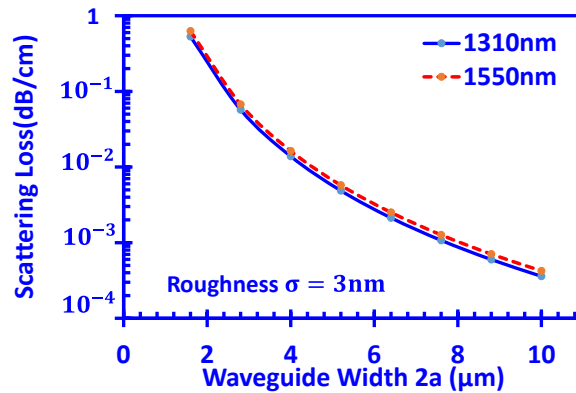


Figure 2-2. Scattering loss as a function of waveguide width  $2a$  for roughness  $\sigma=3\text{nm}$  at  $\lambda=1310$  nm and  $\lambda=1550$  nm.

Figure 2-3 illustrates the scattering loss as function of the waveguide width at various surface roughness ( $\sigma = 3 \text{ nm}$ ,  $\sigma = 5 \text{ nm}$ , and  $\sigma = 8 \text{ nm}$ ) under wavelength  $\lambda=1310\text{nm}$ . As shown in Figure 2-3, the scattering loss will be remarkably suppressed when the surface roughness is reduced to 3 nm. Vice versa, higher level of roughness introduces higher scattering loss. Specifically, the scattering loss induced by side wall roughness in 4  $\mu\text{m}$  wide SOI waveguide is reduced from  $\sim 0.1 \text{ dB/cm}$  to  $\sim 0.014 \text{ dB/cm}$  when  $\sigma$  decreases from 8nm to 3 nm. Such results will be calculated numerically in chapter 3 for comparison.

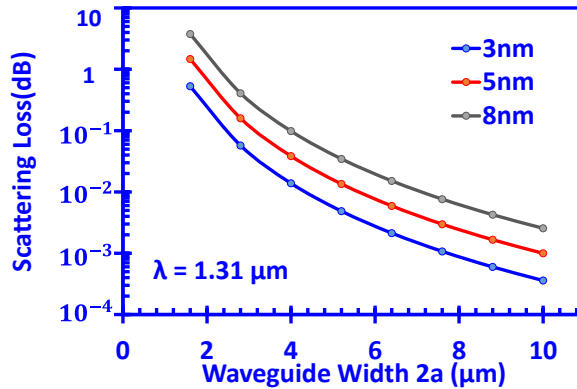


Figure 2-3. Scattering loss versus waveguide width, compare results between  $\sigma = 3 \text{ nm}$ ,  $\sigma = 5 \text{ nm}$  and  $\sigma = 8 \text{ nm}$ , and wavelength is  $\lambda = 1310 \text{ nm}$ . Vertical labels are logarithm.

## 2.2. Waveguide bending loss

In photonic integrated circuits, waveguide bend is used for changing propagation direction of light. However, such bending of waveguide has power leakage due to the coupling of light from guided mode to radiation mode, and eventually degrades the performance of the PIC system. Meanwhile, waveguide bending also causes mode shift, polarization changing, and phase constant changing [5-7]. As the radiation loss is the major power loss source in bending system, we will focus on the analysis of radiation loss for waveguide bending in this section.

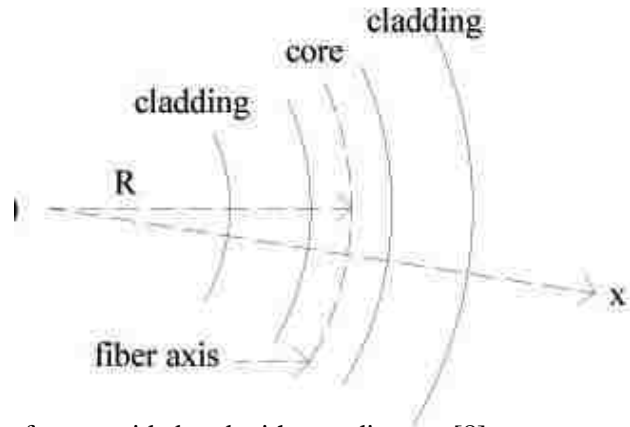


Figure 2-4. Geometry of waveguide bend with coordinate x [8].

Figure 2-4 shows geometry of the waveguide bending, with the bending radius  $R$ . Several modeling methods on waveguide bending loss have been proposed. Tien and co-workers proposed one method analyzing the loss with normalized electrical field [9]. Another analytical model is carried out by Marcatili and Millar [10], in which they showed the bending loss coefficient as equation (2-20).

$$\alpha_{bend} = C_1 \exp(-C_2 R) \quad (2-20)$$

where  $R$  is bending radius, the parameters  $C_1$  and  $C_2$  are constants characterized by waveguide structure and optical mode. These constants are given by:

$$C_1 = \frac{\left(\frac{W}{a}\right)^2}{kn_1(W+1)} \cos(U)^2 \exp(2W) \quad (2-21)$$

and

$$C_2 = \frac{2W\left(\frac{\beta}{k} - n_1\right)}{an_1} \quad (2-22)$$

in which the parameters  $W$  and  $U$  are the normalized parameters as mentioned in section 2.1. With large value of constants  $C_1$  and  $C_2$ , the bending loss can be affected by small change of  $R$ . Specifically, the value of  $\alpha_{bend}$  becomes larger when:

$$R < \frac{1}{C_1} \log C_2 \quad (2-23)$$

Vice versa. Apparently, bending radius is critical to the bending loss coefficient. In that case, to minimize bending loss, the bending radius  $R$  must be big enough. However, in the case of SOI system, the higher refractive index contrast leads to better waveguide confinement, and thus the bending loss is less sensitive to the waveguide bending radius. Therefore, the SOI waveguide allows the bending radius to be in micrometer range. Figure 2-5 represents the calculated result for the bending loss as function of the bending radius.

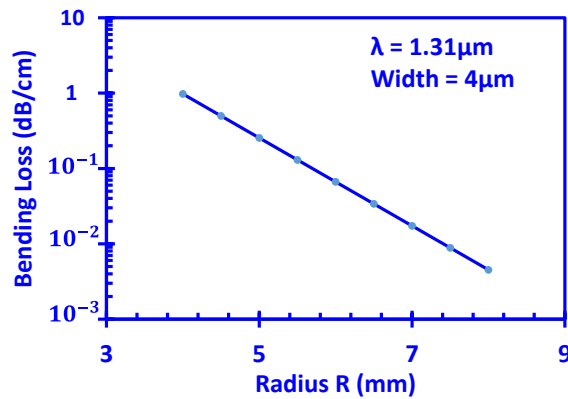


Figure 2-5. Calculated results of bending loss with respect to the bending radius  $R$ , where the wavelength  $\lambda = 1310 \text{ nm}$ , and waveguide width is  $4 \text{ }\mu\text{m}$ .

Figure 2-5 shows the estimated bending loss versus radius  $R$  with the wavelength  $\lambda = 1310 \text{ nm}$  and waveguide width of  $4 \text{ }\mu\text{m}$ , where the loss is plotted in logarithmic scale. The calculated result matches well with the previous prediction. As shown in the figure, the bending attenuation decreases when the bending radius increases. The bending loss can be reduced to as



low as  $\sim 0.017\text{dB/cm}$  when the bending radius  $R$  is approaching to  $\sim 7\text{mm}$ , in which  $0.0187\text{dB}$  per  $90^\circ$  degree waveguide bending. In conclusion, bending loss decreases exponentially when radius  $R$  increases according to the analytical model. Our calculation shows that the SOI system yields the great potential of achieving micrometer scale bending along with remarkable low bending loss.

### 2.3. Tapered Waveguide

Tapered waveguide - a type of waveguide with slowly varying width- was designed to connect two uniform waveguides with different dimensions. Such waveguide structure allows the conversion of the mode size from  $W_1$  (entry point) to another mode size  $W_2$  (exit point), as shown in figure 2-8. Some literatures have reported the studies of such tapered waveguide in different methods, for examples: Matsumaru [11] reported on the reflections in non-uniform transmission lines, Chakraborty [12] found the transmission matrix of tapered waveguide after divided it into finite sections. To express the concept clearly, one model describing the transmission property in a linear tapered waveguide transmission in this section is presented in this section following the same treatment proposed in the literatures [13, 14].

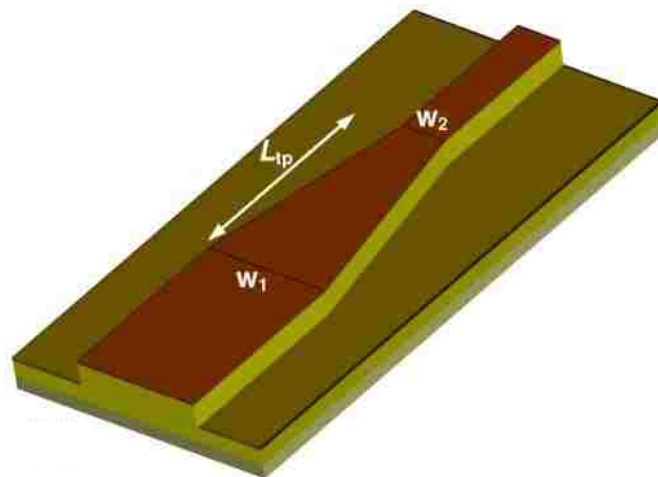


Figure 2-6. Configuration of a regular lateral tapered waveguide [15].

Figure 2-6 represents a linear tapered waveguide with a varying waveguide width for a fixed length of  $L$  and a constant height. For the tapered waveguide, Maxwell's equation becomes very complicated. In that case, we choose to use finite differential method for solving the power transmission in a tapered waveguide.

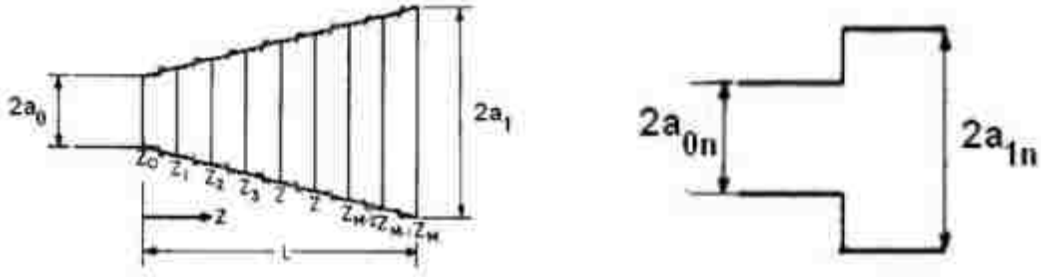


Figure 2-7. Slowing varying waveguide [16].

Dividing the tapered waveguide into  $N$  sections with uniform length of  $\Delta x = L/N$ , the tapered waveguide can be treated as the linear combination conventional waveguides with linearly increased width. Figure 2-7 shows the differentiated tapered waveguide, in which two adjoined waveguides have the width of  $2a_1$  and  $2a_0$  respectively. In this model, the linear change in waveguide width can be expressed as equation (2-24).

$$a(x) = a_0 + \frac{a_1 - a_0}{L} x \quad (2-24)$$

When the waveguide width discontinuity between each waveguide sections is relatively small, a well-known equation for reflection coefficient can be used as  $R = \frac{Z_b - Z_a}{Z_b + Z_a}$  [17]. The  $Z_a$  and  $Z_b$  represent the impedances of two adjacent waveguide sections. Knowing the reflection of each interface, the total reflection coefficient can be obtained. In this section, we follow the treatment developed by the literatures [13, 14] for a two dimensional tapered waveguide with fundamental

mode  $TE_0$ , and the multi-reflection is neglected in the analysis. Eventually the total reflection can be expressed as following:

$$R = R_1 \exp(-2i\beta_0\Delta x) + R_2 \exp(-2i\beta_0\Delta x - 2i\beta_1\Delta x) + \dots + R_N \exp(-2 \sum_{m=0}^{N-1} i\beta_m\Delta x) \quad (2-25)$$

where the  $\beta_i$  in the equation is propagation constant in  $i$ -th waveguide sections. As proposed in the literature, this equation can be simplified as:

$$R \approx \sum_{n=1}^N R_N \exp(-2 \sum_{m=0}^{N-1} i\beta_m\Delta x) \quad (2-26)$$

where  $R_N$  is the reflection coefficient at  $N$ -th section.

$$R_N = \frac{Z_n - Z_{n-1}}{Z_n + Z_{n-1}} \quad (2-27)$$

Assuming the  $N$  is approaching infinity, the total reflection coefficient can be expressed with integration:

$$R = \frac{1}{4i\beta_0} \left( \frac{d}{dx} \ln Z \right)_0 - \frac{1}{4i\beta_1} \left( \frac{d}{dx} \ln Z \right)_1 \exp(-2 \int_0^L i\beta dx) \quad (2-28)$$

In this equation, the subscription 0 and 1 represent the two waveguide channels connected to the input port and out port of tapered waveguide respectively. With  $TE_{10}$  mode, propagation constant  $\beta$  will be:

$$\beta^2 = k^2 - \left( \frac{\pi}{a} \right)^2 \quad (2-29)$$

Where the wavenumber  $k = 2\pi n/\lambda$ , determined by the refractive index  $n$ , and free space wavelength  $\lambda$ . Then  $\beta$  can be simplified as:

$$\beta = \frac{2\pi}{\lambda} \sqrt{1 - \left( \frac{\lambda}{2a} \right)^2} \quad (2-30)$$

Having impedance equation [17]:

$$Z = \frac{\pi\eta_0}{2} \frac{b}{a\sqrt{1-(\frac{\lambda}{2a})^2}} \quad (2-31)$$

where  $\eta_0$  is the impedance in free space, given as  $\eta_0 = \sqrt{\mu_0/\epsilon_0}$ . Substituting those parameter into reflection coefficient equation [17]:

$$|R| = \frac{\lambda}{L} \sqrt{\frac{K_0^2 + K_1^2}{64\pi^2} - \frac{K_0 K_1}{32\pi^2} \cos(4\pi l)} \quad (2-32)$$

where

$$K_0 = -\frac{(a_1 - a_0)/a_0}{(1 - (\frac{\lambda}{2a})^2)^{3/2}} \quad (2-33)$$

$$K_1 = -\frac{(a_1 - a_0)/a_1}{(1 - (\frac{\lambda}{2a})^2)^{3/2}} \quad (2-34)$$

$$l = \int_0^L \frac{dx}{\lambda_g} = \frac{1}{\lambda} \int_0^L \sqrt{1 - (\frac{\lambda}{2a})^2} dx \quad (2-35)$$

Neglecting the absorption inside the waveguides, the transmittance will be 1-R. *Figure 2-8* shows the transmittance of a tapered waveguides as function of taper length. In this calculation, the tapered waveguide structure is silicon on top of silica waveguide with the output port width  $2a_1 = 9.5\mu\text{m}$ , and input port width  $2a_0 = 4\mu\text{m}$ . The wavelength is assumed to be  $\lambda = 1.31\mu\text{m}$ . As shown in *figure2-8*, the input power of the tapered waveguide is normalized to 1. The transmitted power of tapered waveguide increased first as the taper length increases to around  $50\mu\text{m}$ . Afterwards, the transmittance starts to oscillate when taper length is larger than  $50\mu\text{m}$ . Generally speaking, transmittance becomes closer to unit when taper length increases. According to the

analytical results, the total taper coupling loss in a tapered waveguide structure can reach 0.0017dB when taper length is 220  $\mu\text{m}$ .

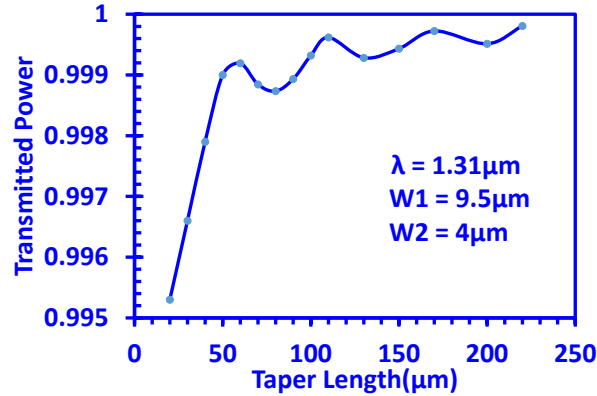


Figure 2-8. Transmittance versus taper length, where the taper structure is silicon on top of silica, with  $TE_0$ ,  $\lambda = 1.31\mu\text{m}$ , and  $2a_1 = 9.5\mu\text{m}$ ,  $2a_0 = 4\mu\text{m}$ .

## 2.4. Coupler structure

Coupler is an important component in PIC system, which is a four-port devices, in which the operation relies on distributed coupling between two individual waveguides close to one another. As shown in Figure 2-9, the coupler with the same waveguide, is called symmetric coupler, where the waveguide width is represented as  $2a$ , and the distance between two waveguides is called coupler spacing  $S$ . The figure also introduces a coordinate for following analysis. The  $z$  axes is the propagation direction along waveguides and  $x$  axes represent transversal plane for waveguides. Based on this coordinate, analysis using coupled mode theory is presented in this section for coupling between the two identical waveguides. Our analysis follows the same treatment developed by literature [18].

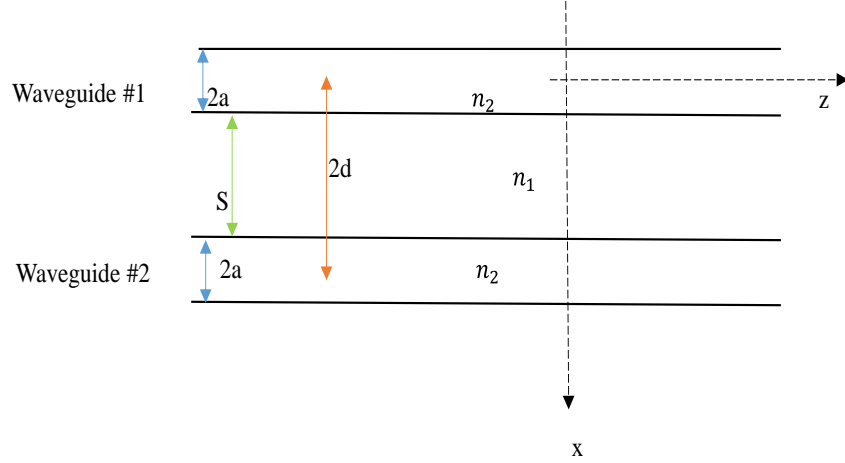


Figure 2-9. Schematic diagram of the coordinate axes for the analysis of parallel waveguides.  $2a$  is waveguide width in  $y$  direction,  $S$  is spacing between two waveguides,  $2d$  is distance between centers of two parallel waveguides. Put coordinate axes at center of waveguide #1.

In this section, we assume both waveguides of the coupler are single mode, and coupling happens between two identical waveguides without any diffraction. Considering electromagnetic field of coupled waveguide is sum of two eigenmodes in each waveguide, the field can be represented as following:

$$\begin{cases} E = A(z)E_1 + B(z)E_2 \\ H = A(z)H_1 + B(z)H_2 \end{cases} \quad (2-36)$$

Where  $A(z)$  and  $B(z)$  are amplitude of field in two adjacent waveguides that exchange power along with propagation length  $z$ .

According to Maxwell's equation, the electromagnetic field satisfies equations as:

$$\nabla \times E = -j\omega\mu H \quad (2-37)$$

$$\nabla \times H = j\omega\epsilon E \quad (2-38)$$

Substituting equations, we can obtain:

$$(z \times E_1) \frac{dA}{dz} + (z \times E_2) \frac{dB}{dz} = 0 \quad (2-39)$$

$$(z \times H_1) \frac{dA}{dz} - j\omega(\varepsilon_r - \varepsilon_1)AE_1 + (z \times E_2) \frac{dB}{dz} - j\omega(\varepsilon_r - \varepsilon_2)BE_2 = 0 \quad (2-40)$$

Substituting equation (2-39) and (2-40) into coupled-mode equation:

$$\iint [E_1^*(Eq(2-40)) - H_1^*(Eq(2-39))]dxdy = 0 \quad (2-41)$$

$$\iint [E_2^*(Eq(2-40)) - H_2^*(Eq(2-39))]dxdy = 0 \quad (2-42)$$

After simplification, we can have [18]:

$$\frac{dA}{dz} + C_{12} \frac{dB}{dz} e^{-j(\beta_2 - \beta_1)z} + j\chi_1 A + jk_{12} B e^{-j(\beta_2 - \beta_1)z} = 0 \quad (2-43)$$

where  $C_{12}$  is butt coupling coefficient,  $\chi_1$  is the change in propagation constant, and  $k_{12}$  is mode coupling coefficient. Equation 2-43 is a description of EM field in waveguide #1. We can also obtain similar formula for waveguide #2. Mode coupling coefficient here can be expressed as [18]:

$$k_{12} = \frac{\omega \varepsilon_0 \iint (\varepsilon_r - \varepsilon_{r,1}) E_1^* E_2 dxdy}{\iint z (E_1^* \times H_1 + E_2^* \times H_2) dxdy} \quad (2-44)$$

where  $\varepsilon_r$  is dielectric constant as  $\varepsilon_r = n^2$ , and  $\varepsilon_{r,1}$  is dielectric constant of waveguide #1. Considering fundamental TE<sub>0</sub> mode in the waveguide, components  $E_x$  and  $H_y$  always equal to 0, and  $H_x = -\left(\frac{\beta}{\omega\mu}\right)E_y$ . Electrical field  $E_y$  can be represented by normalized parameters, U, W as described in former sections, with coordinate axis showed in *Figure 2-9*.

$$E_{1y} = \begin{cases} A \cos\left(\frac{U}{a}x\right), & |x| \leq a \\ A \cos(U) \exp\left(-\frac{W}{a}(|x| - a)\right), & |x| > a \end{cases} \quad (2-45)$$

$$E_{2y} = A \cos(U) \exp\left(\frac{W}{a}(x - 2d + a)\right), \text{ when inside waveguide \#2} \quad (2-46)$$

Substituting electrical field into coupling coefficient formula:

$$k_{12} = \frac{k_0^2}{\beta} (n_2^2 - n_1^2) \frac{U^2 W^2}{(1+W)V^4} \exp\left(-\frac{W}{a} (2d - a)\right) \quad (2-47)$$

With mode coupling coefficient formula, we can have a numerical simulation for SOI based waveguide coupler, in which the refractive index in silicon core  $n_2 = 3.5$ , and the refractive index in silica cladding is  $n_1 = 1.5$ . The calculated results are plotted versus spacing  $S$  between two waveguides in Figure 2-10.

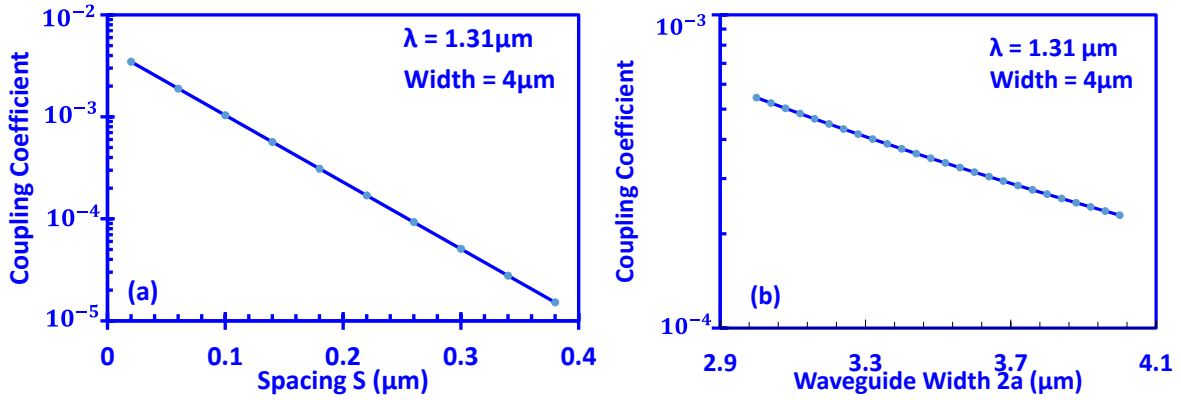


Figure 2-10. Figure (a) shows logarithm plot of coupling coefficient as function of waveguide spacing  $S$ , when waveguide width  $@2a=4 \mu\text{m}$ . Figure (b) shows logarithm plot of coupling coefficient as function of waveguide width, when spacing between two waveguides is  $S=0.2 \mu\text{m}$ . Both results is  $@ \lambda = 1.31 \mu\text{m}$ .

In Figure 2-10, the numerical results show that mode coupling coefficient  $k_{12}$  reduces exponentially with spacing  $S$  increases, and exponentially reduces with waveguide width  $2a$  increases. To reach high coupling efficiency, two waveguides should be placed be as close as possible. Because a smaller waveguide has bigger evanescent field outside of the core, it relatively has higher  $k_{12}$ .

Assuming no loss during coupling, electrical field in each waveguides can be expressed as:

$$E_1 = i \sin(k_{12}z) \psi_1 \quad (2-48)$$



$$E_2 = \cos(k_{12}z)\psi_2 \quad (2-49)$$

where  $\psi$  represents normalized eigenmode. Since field energy is proportional to  $E^2$ , the power exchange between two waveguides is represented in *Figure 2-11 (a)*.

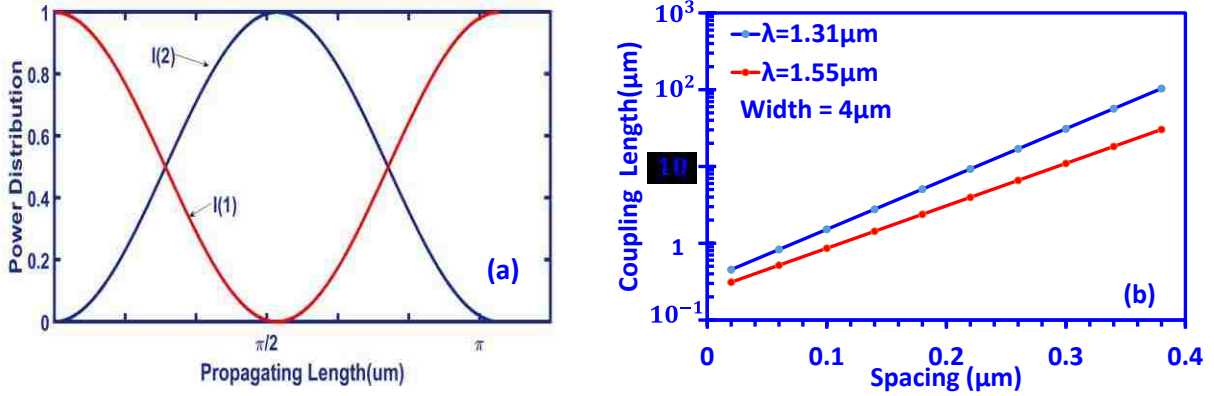


Figure 2-11 (a): Power distribution of two waveguides varies along propagating direction. (b): logarithm plot of complete coupling length as function of waveguide spacing, @  $\lambda = 1.31\mu\text{m}$  and  $\lambda = 1.55\mu\text{m}$ , where waveguide width is  $2a = 4\mu\text{m}$ , and coupling length is in unit of mm.

Complete power transfer happens when  $kz = \pi/2$  with as shown in *Figure 2-11(a)*. *Figure 2-11 (b)* illustrate the coupling length versus waveguide spacing. As showed in *Figure 2-11 (b)*, coupling length increases exponentially as spacing between waveguides increases. The results in *Figure 2-11 (b)* are calculated on a symmetric directional coupler, where waveguide has refractive index:  $n_{core} = 3.5, n_{cladding} = 1.5$ . The waveguide in the coupler has width= $4\mu\text{m}$ , and the operating wavelength is set to  $\lambda = 1.31\mu\text{m}$  and  $\lambda = 1.55\mu\text{m}$  respectively. The figure compares coupling length at different wavelengths. For example, while spacing  $S=0.3\mu\text{m}$ , 30mm coupling length is needed for one complete power coupling at  $\lambda = 1.31\mu\text{m}$ , while 10mm coupling length is needed at  $\lambda = 1.55\mu\text{m}$ . Coupling length in a symmetric directional coupler at  $\lambda = 1.31\mu\text{m}$  is slightly higher than that at  $\lambda = 1.55\mu\text{m}$ .

## 2.5. Intersection crosstalk

For PIC networks, small dimension and high integration is desired for portable devices. To achieve high level of integration, optimized intersection is required to make two photonic integrated circuits overlap with each other without crosstalk.

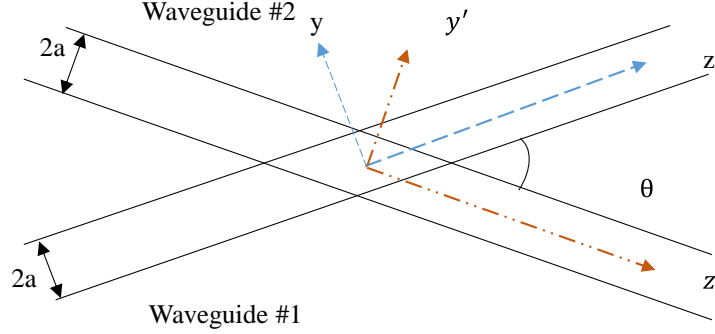


Figure 2-12. Schematic diagram of coordinate axes for analysis of intersecting waveguides.

In this section, analysis of crosstalk based on coupled mode theory is presented for linear intersected waveguides following the same treatment proposed by the literatures [13, 19, 20]. As shown in figure 2-12, when two waveguides intersect in a small angle, crosstalk happens attributed to the overlap of evanescent fields when the two waveguides are getting closer. Then light couples from one waveguide to the other. Assuming two identical intersecting waveguides in which the refractive index of core and cladding layer are the same, the normalized  $TE_0$  mode eigenfunction  $\psi(y, z)$  for each waveguide is given as [13]:

$$\psi(y, z) = \begin{cases} \frac{\sqrt{2\omega\mu_0}e^{-\gamma(y-a)}e^{j\beta z}}{\sqrt{\beta(a+\frac{1}{\gamma})(1+\frac{\gamma^2}{\alpha^2})}}, & \text{for } +a \leq y \leq \infty \\ \frac{\sqrt{2\omega\mu_0}\cos(\alpha y)e^{j\beta z}}{\sqrt{\beta(a+\frac{1}{\gamma})}}, & \text{for } -a \leq y \leq +a \\ \frac{\sqrt{2\omega\mu_0}e^{\gamma(y+a)}e^{j\beta z}}{\sqrt{\beta(a+\frac{1}{\gamma})(1+\frac{\gamma^2}{\alpha^2})}}, & \text{for } -\infty \leq y \leq -a \end{cases} \quad (2-50)$$

Where symbols  $\alpha$  and  $\gamma$  are normalized parameters as  $\alpha = U/a$ ,  $\gamma = W/a$ .  $U$  and  $W$  are introduced in former sections. In core region ( $-a \leq y \leq +a$ ), mode field is cosine shape, while in cladding region electrical field vanishes along  $y$  direction in exponential shape.

The coordinate axes for two waveguides,  $(y,z)$  and  $(y',z')$  can be converted to each other as [20]:

$$\begin{cases} y' = -\sin\theta \cdot z + \cos\theta \cdot y \\ z' = \cos\theta \cdot z + \sin\theta \cdot y \end{cases} \quad (2-51)$$

Then, coupling coefficient is given by the ratio of light coupling to waveguide #2 over initial light in waveguide #1:

$$K = \frac{E_2(y',z')}{E_1(y,z)} = \frac{\omega}{4} \iint [\epsilon(y,z) + \iota(y,z)] \times \psi_2(y',z')\psi_1(y,z) dydz \quad (2-52)$$

This treatment has been developed and derived by Agrawal, N. and his coworkers [13, 21]. The  $\epsilon(y,z)$  represents dielectric constant for two single-mode waveguides, and  $\iota(y,z)$  denotes changing from  $\epsilon(y,z)$  in intersecting region.

$$\epsilon(y,z) = \begin{cases} \epsilon_0(n_2^2 - n_1^2), & -a \leq y \leq +a \\ 0, & \text{otherwise} \end{cases} \quad (2-53)$$

$$\iota(y,z) = \begin{cases} -\epsilon_0(n_2^2 - n_1^2), & -a \leq y' \leq +a \\ 0, & \text{otherwise} \end{cases} \quad (2-54)$$

Then, coupling coefficient  $K$  can be simplified as [13]:

$$K = \frac{k_0(n_2^2 - n_1^2)}{\beta(a + \frac{1}{\gamma})\sqrt{1 + \frac{\gamma}{\alpha}[\gamma^2 + \beta^2 \tan^2(\frac{\theta}{2})]}\sin\theta} \left\{ \gamma \sin \left[ \beta \tan \left( \frac{\theta}{2} \right) a \right] - \beta \tan \left( \frac{\theta}{2} \right) \cos \left[ \beta \tan \left( \frac{\theta}{2} \right) a \right] \right\} \times \left( \frac{\sin \left\{ \left[ \alpha - \beta \tan \left( \frac{\theta}{2} \right) \right] a \right\}}{\left[ \alpha - \beta \tan \left( \frac{\theta}{2} \right) \right]} + \frac{\sin \left\{ \left[ \alpha + \beta \tan \left( \frac{\theta}{2} \right) \right] a \right\}}{\left[ \alpha + \beta \tan \left( \frac{\theta}{2} \right) \right]} \right) \quad (2-55)$$

where  $k_0$  is wavenumber in free space,  $\theta$  is the crossing angle. When  $\frac{\theta}{2} = \text{atan}\left(\frac{\beta}{\alpha}\right)$ , optical rays in two waveguides would be parallel for half of the bounce distance, which is quasi-phase-matching condition. In that case, when  $\alpha = \beta \tan(\theta/2)$ ,

$$\gamma \sin \left[ \beta \tan \left( \frac{\theta}{2} \right) a \right] - \beta \tan \left( \frac{\theta}{2} \right) \cos \left[ \beta \tan \left( \frac{\theta}{2} \right) a \right] = 0 \quad (2-56)$$

Coupling coefficient  $K$  would be 0, which means no energy being coupled when waveguide crossing angle  $\theta = 2 \text{atan}\left(\frac{\beta}{\alpha}\right)$ .

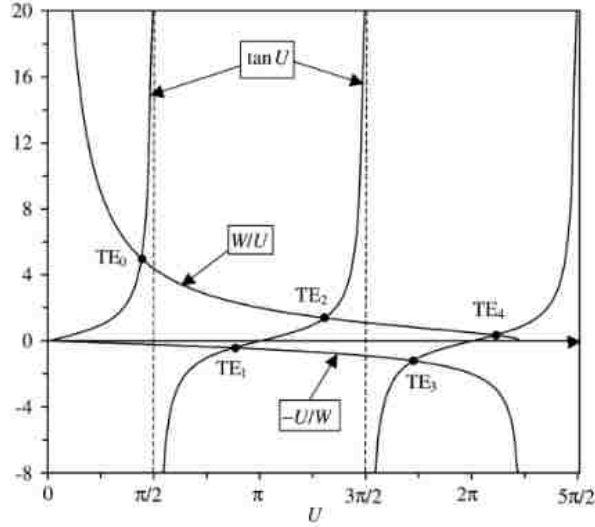


Figure 2-13 Eigenvalue of TE mode, even mode have relation of  $\tan U = \frac{W}{U}$ , and odd mode have relation function:  $\tan U = -U/W$ , and the black spots denote parameter  $U$  for a specific waveguide structure[14].

To determine parameters for  $TE_0$  mode, dispersion relation is solved graphically as shown in figure 2-13 [14]:

$$\tan U = \frac{W}{U} \quad (2-57)$$

where the normalized parameters  $V$  and  $W$  is the same as reviewed in equation 2-8 and 2-9, and  $U$  is solved graphically as shown in figure 2-13. Afterwards the propagation constant  $\beta$  can be solved using following equation:

$$\beta = \sqrt{k_0^2 n_2^2 - \left(\frac{U}{a}\right)^2}. \quad (2-58)$$

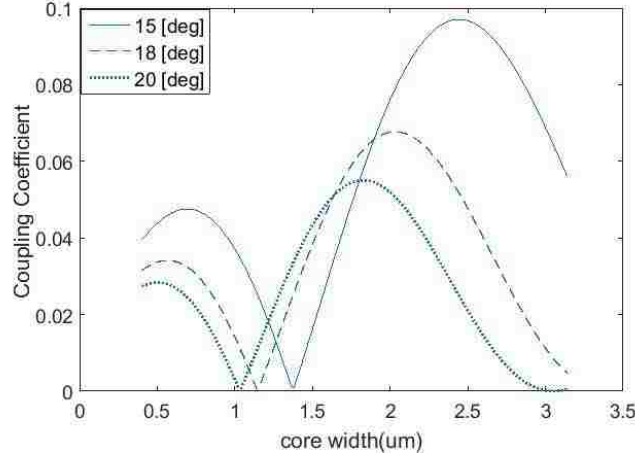


Figure 2-14 Coupling coefficient as function of core width  $2a$  [ $\mu\text{m}$ ] for crossing angles at 15, 18 and 20 degree, respectively. The waveguide structure has silicon core with  $n_2=3.5$ , and silica cladding layer with  $n_1=1.5$  with operating wavelength  $\lambda = 1.31\mu\text{m}$ .

Numerical analysis from Figure 2-14 has showed that the coupling coefficient  $K$  resonances when core width increases. Such property is corresponding to Sinc function in  $K$ 's formula due to the effect of quasi phase-matching. At the same time, coupling coefficient decreases when crossing angle  $\theta$  increase, which equivalent to  $(\sin\theta)^{-1}$  dependence of  $K$ . With coupling coefficient  $K$  solved, the crosstalk power transferred from waveguide #1 to waveguide #2 can be described as:

$$P = K^2 \quad (2-59)$$

Thus the crosstalk power in dB between two waveguides versus intersecting angles is shown in Figure 2-15.

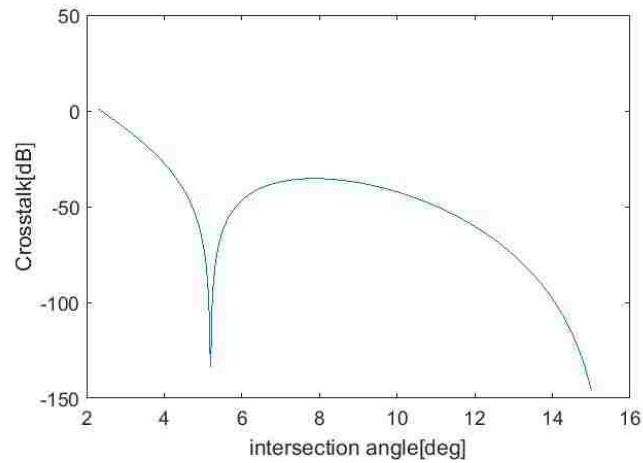


Figure 2-15. Crosstalk power in dB from waveguide #1 to waveguide #2 as function of intersection angle, where  $a=2\mu\text{m}$ ,  $\lambda = 1.31\mu\text{m}$ .

When the core width is fixed, phase matching condition happens only one time while crossing angle is changing. In that case, no crosstalk happens as showed in *Figure 2-15*. In this section, results only show two dimensional waveguides with small crossing angles, and no reflections and scattering are taken into consideration. Chapter 3.6 will introduce 3D waveguide crossing with more complex configuration using Lumerical FDTD Solutions simulation tool, which will give more accurate results.

## References for chapter 2

1. Grillot, F., et al., *Size influence on the propagation loss induced by sidewall roughness in ultrasmall SOI waveguides*. IEEE Photonics Technology Letters, 2004. **16**(7): p. 1661-1663.
2. Bogaerts, W., P. Bienstman, and R. Baets, *Scattering at sidewall roughness in photonic crystal slabs*. Optics letters, 2003. **28**(9): p. 689-691.
3. Payne, F. and J. Lacey, *A theoretical analysis of scattering loss from planar optical waveguides*. Optical and Quantum Electronics, 1994. **26**(10): p. 977-986.
4. Grillot, F., et al., *Propagation loss in single-mode ultrasmall square silicon-on-insulator optical waveguides*. Journal of lightwave technology, 2006. **24**(2): p. 891.
5. Kumar, A., R. Jindal, and R.L. Gallawa, *Bending induced phase shifts in arbitrarily bent rectangular-core dual-mode waveguides*. Journal of lightwave technology, 1996. **14**(2): p. 196-201.
6. Reed, G.T., *Silicon Photonics: the state of the art*. 2008: John Wiley & Sons.
7. Sakai, A., T. Fukazawa, and T. Baba, *Estimation of polarization crosstalk at a micro-bend in Si-photonic wire waveguide*. Journal of lightwave technology, 2004. **22**(2): p. 520.
8. Yao, L., T. Birks, and J.C. Knight, *Low bend loss in tightly-bent fibers through adiabatic bend transitions*. Optics express, 2009. **17**(4): p. 2962-2967.
9. Tien, P., *Light waves in thin films and integrated optics*. Applied Optics, 1971. **10**(11): p. 2395-2413.
10. Marcatili, E., *Bends in optical dielectric guides*. Bell System Technical Journal, 1969. **48**(7): p. 2103-2132.
11. Matsumaru, K., *Reflection coefficient of E-plane tapered waveguides*. Microwave Theory and Techniques, 1958: p. 143-149.
12. Chakraborty, *Transmission matrix of a linear double taper in rectangular waveguides*. IEEE Trans. Microw. Theory Tech., 1980: p. 577-579.
13. Agrawal, N., L. McCaughan, and S. Seshadri, *A multiple scattering interaction analysis of intersecting waveguides*. Journal of applied physics, 1987. **62**(6): p. 2187-2193.
14. Bures, J., *Guided optics*. 2009: John Wiley & Sons.
15. Dai, D., Y. Tang, and J.E. Bowers, *Mode conversion in tapered submicron silicon ridge optical waveguides*. Optics express, 2012. **20**(12): p. 13425-13439.
16. Dwari, S., A. Chakraborty, and S. Sanyal, *Analysis of linear tapered waveguide by two approaches*. Progress In Electromagnetics Research, 2006. **64**: p. 219-238.
17. Johnson, R., *Design of linear double tapers in rectangular waveguides*. IRE Transactions on Microwave Theory and Techniques, 1959. **7**(3): p. 374-378.
18. Rumpf, R.C., *Lecture #5 Coupled-Mode Theory*.
19. McCaughan, L., N. Agrawal, and G. Bogert, *Novel physical effects in intersecting waveguides*. Applied physics letters, 1987. **51**(18): p. 1389-1391.
20. Kobayashi, Y. and H. Tsuda, *Crosstalk reduction using tapered intersecting waveguides*. Optical review, 2005. **12**(5): p. 387-390.
21. Agrawal, N., *Novel physical effects in intersecting optical waveguides*. 1988.

### 3. Numerical simulation on loss analysis and optimization

In chapter 3, we focus on design and simulating all the optical components which have been introduced in chapter 2. In this chapter, the Finite-Difference Time-Domain (FDTD) method is reviewed firstly for calculating the Maxwell's equations. The Lumerical FDTD solutions will be utilized as the simulation tool. Furthermore, simulation of each structure was carried out based on the silicon-on-insulator (SOI) structure at wavelength  $\lambda=1.31\mu\text{m}$ . At last, an optimized design for a PIC structure with low optical loss is presented for optical-coherence-tomography (OCT) system application.

#### 3.1. Introduction of Finite-Difference-Time-Domain (FDTD) method

FDTD method is one of the most popular techniques for solving electromagnetic problems. In a complicated geometry structure, solving Maxwell's equations analytically needs massive calculation and is very time consuming. FDTD method is a simple and efficient numerical method for calculating light propagation problem. Specifically, FDTD discretizes both of the time and space domain into finite numbers of cells, and then solves the Maxwell's equations in each cell. Equation (3-1) shows the Maxwell's equation,

$$\begin{cases} \frac{\partial E}{\partial t} = \frac{1}{\epsilon_0} \nabla \times H \\ \frac{\partial H}{\partial t} = -\frac{1}{\mu_0} \nabla \times E \end{cases} \quad (3-1)$$

In one dimensional model, an electromagnetic wave traveling along z-direction has two components of  $E_x$  and  $H_y$ . By using the central difference approximation [1], the Maxwell's equations can be converted to:



$$\begin{cases} \frac{E_x^{n+\frac{1}{2}}(k) - E_x^{n-\frac{1}{2}}(k)}{\Delta t} = -\frac{1}{\epsilon_0} \frac{H_y^n(k+\frac{1}{2}) - H_y^n(k-\frac{1}{2})}{\Delta z} \\ \frac{H_y^{n+1}(k+\frac{1}{2}) - H_y^n(k+\frac{1}{2})}{\Delta t} = -\frac{1}{\mu_0} \frac{E_x^{n+\frac{1}{2}}(k+1) - E_x^{n+\frac{1}{2}}(k)}{\Delta z} \end{cases} \quad (3-2)$$

From formula 3-2, the time derivative of E field at time  $n\Delta t$  can be expressed by E field at times  $(n+1/2)\Delta t$  and  $(n-1/2)\Delta t$ . Also, the space derivative of H field at point  $k\Delta x$  can be derived by  $(k+1/2)\Delta x$  and  $(k-1/2)\Delta x$ . By solving the Maxwell's equation in finite numbers of time and space unit cell, the propagation of light can be revealed by the value of  $E_x$  and  $H_y$  in each cell. Figure 3-1 shows the schematic of Yee's method for solving 1-D EM field in both space and time domain [2]. In three dimensional case, the Yee's cell can be represented as Figure 3-2 [3].

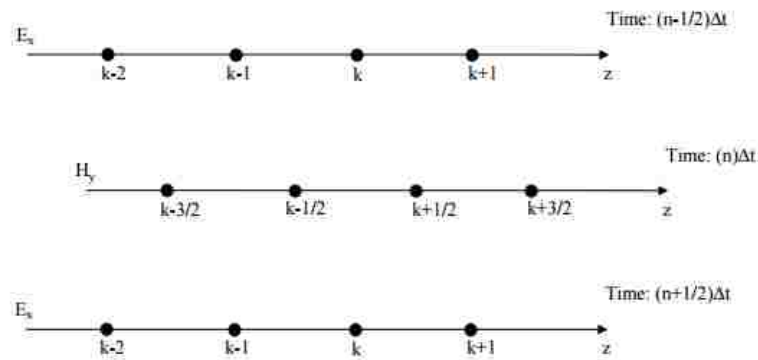


Figure 3-1. Schematic of Yee's 1-D EM field with space and time reference[2].

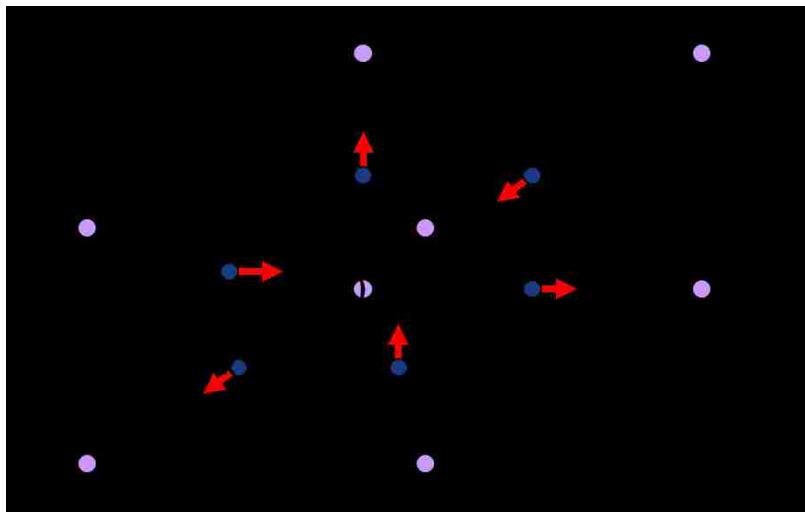


Figure 3-2. Three-dimensional of Yee's EM field cell[3].

### 3.2. Surface roughness

Optical waveguide technology has been improved and advanced allowing high performance optical devices for various applications [4]. However, as waveguide dimension decreases, some problems induced by the imperfect fabrication process become significant for optical efficiency, especially in the silicon-on-insulator (SOI) waveguide. SOI waveguide, benefiting from large refractive index contrast, is able to confine electromagnetic field strongly inside the core region. The SOI structure also allows waveguide dimension to be submicron magnitude [5, 6]. Due to the imperfect etching process, SOI waveguide suffers from sidewall roughness which caused one fundamental propagation loss in SOI-based-devices.

To predict the effect of surface roughness on propagation loss in a SOI waveguide, we have reviewed an analysis model developed by Payne and Lacey[7]. Based on analytical results shown in chapter 2, scattering loss induced by sidewall roughness is the function of waveguide dimension and roughness dimension. Such analytical model have also been developed on both 2-D and 3-D SOI waveguide[8, 9], and experimentally measured[10]. So in this section, we focus on obtaining accurate scattering loss of 3-D SOI waveguide by applying FDTD simulation. All simulation results are calculated at wavelength  $\lambda = 1.31\mu m$ .

To describe the waveguide sidewall roughness in Lumerical FDTD solution, we use the same autocorrelation model reviewed in Chapter 2 [7]. The autocorrelation function (ACF) describes the roughness with respect to flat surface by correlating intensity of each random point with equation  $R(u)$ , in which the  $\sigma^2$  is mean-square deviation representing for roughness,  $L_c$  is the correlation length.

$$R(u) = \sigma^2 \exp\left(-\frac{|u|}{L_c}\right) \quad (3-3)$$

In order to generate roughness, a matrix of random numbers in k-space with coordinate x-y, and the surface of sidewall is defined by a n by m matrix, and the height of each point on the surface is given as a function of x and y. Applying ACF relation to the matrix in k-space, surface roughness in real space then follows the treatment proposed by Payne and Lacey [7]. K-space is the Fourier transform of the real space. Every point in k-space represents a complex number of frequency and phase. [11].

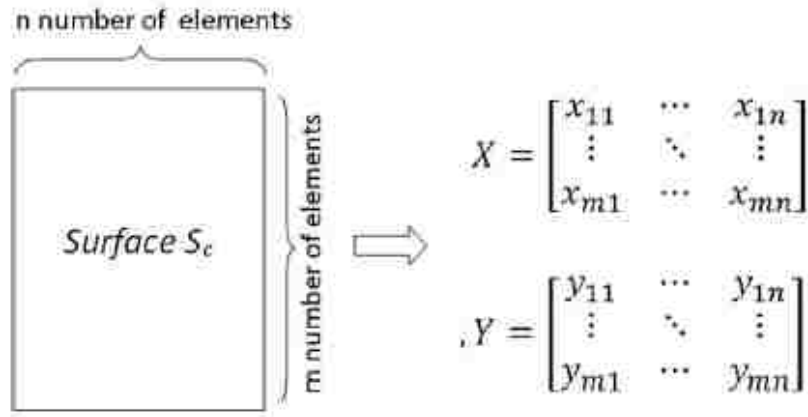


Figure 3-3. X and Y matrix containing n by m elements representing discrete in real space[11].

Applying the ACF relation, we calculate scattering loss with various root mean square (RMS)  $\sigma$  and waveguide widths. For example, the scattering loss in a ridge SOI waveguide with height of  $4.5\mu\text{m}$  and width of  $4\mu\text{m}$  is  $0.00124 \text{ dB}/\mu\text{m}$  when the roughness parameter  $L_c = 20\text{nm}$  and  $\sigma=13\text{nm}$ . Figure 3-4 shows the calculated scattering loss versus waveguide width. The simulation result follows the same trend as shown in the analytical model. The scattering loss reduces exponentially when the waveguide width increases.

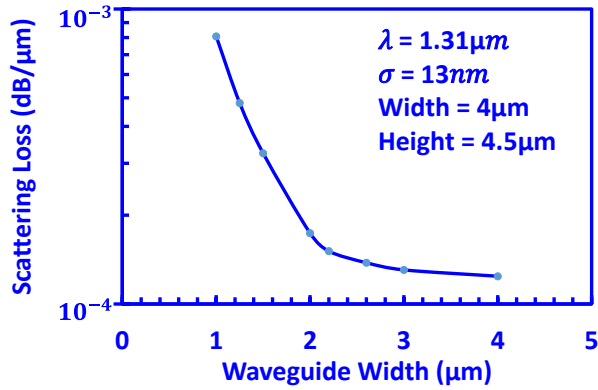


Figure 3-4. Calculated scattering loss as a function of waveguide width ( $\mu\text{m}$ ), with waveguide height= $4.5 \mu\text{m}$ ,  $\lambda = 1.31 \mu\text{m}$ , correlation length  $L_c = 20 \text{nm}$ . The plot is in logarithmic scale.

### 3.3. Bend design

Waveguide bending is a mostly used fundamental element in photonic integrated circuits for redirect propagation of light. Figure 3-5 shows a 3-D model in the Lumerical FDTD Solutions for a SOI based ridge waveguide bending, where the red portion represents silicon and blue portion represents silicon-oxide substrate. In waveguide bending, the bending loss is induced by ray leakage, which is the leakage of light from core region to cladding layer when the mode field shifts in the bending section. Such optical loss is called radiation loss. In addition to the radiation loss, the transition loss caused by modal mismatch between the bent waveguide and straight waveguide is another loss source. Such loss is also caused by mode field shift when waveguide bending connects with straight waveguide. Thus, in order to simulate the transition loss, straight waveguide is also added along with the bending section to calculate the total loss induced by waveguide bending. Considering the loss sources, magnitude of bending loss depends on the bend radius and waveguide confinement.

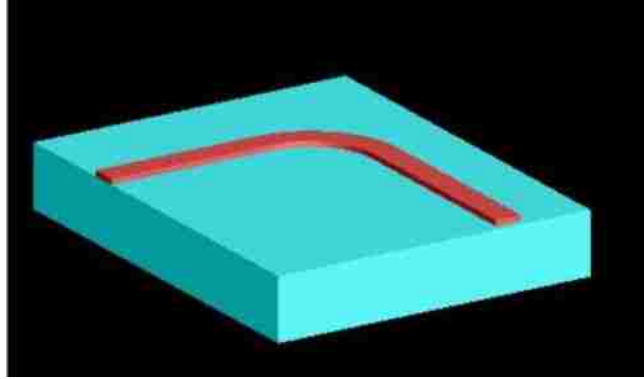


Figure 3-5. Schematic of waveguide bend in SOI [12].

In chapter 2, we have reviewed the impact of bending radius on the waveguide bending loss by using Marcatili's model [13]. However, such analytical method can only estimate the radiation loss. In this section, we numerically analyze the waveguide bendings with the Lumerical FDTD solutions simulation tool. In our simulation, we set up a  $90^\circ$  ridge waveguide bending section with height of  $4.5\ \mu\text{m}$  and width of  $4\ \mu\text{m}$ . Figure 3-6 shows the simulation results of both radiation loss and transition loss versus radius of bending at wavelength of  $1.31\ \mu\text{m}$ . The figure shows that the total loss reduces while the bending radius is increasing. At about  $2000\ \mu\text{m}$ , radiation loss goes to  $0.1\text{dB}$ .

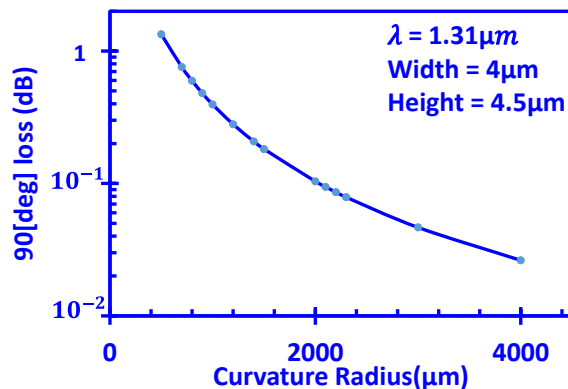


Figure 3-6. Transmittance of 90-degree waveguide bending versus curvature radius ( $\mu\text{m}$ ), the waveguide dimension is width at  $4\ \mu\text{m}$  and height of  $4.5\ \mu\text{m}$ . A comparably low radiation loss can be achieved at radius =  $2000\ \mu\text{m}$ .

In order to suppress radiation loss and transition loss due to modal mismatch in waveguide bending, various approaches have been proposed. For example, placing air trench for reflecting light from waveguide-air interface [14, 15], or shift waveguide to correct modal mismatch [16]. Because the air trench will occupy a large space on the circuit board, the second method, i.e. lateral offset for reducing bending loss, will be studied in this section. Figure 3-7 shows a  $90^\circ$  waveguide bending section with lateral offset, in which the optical mode propagates in x-z plane and is transversely confined in x-y plane.

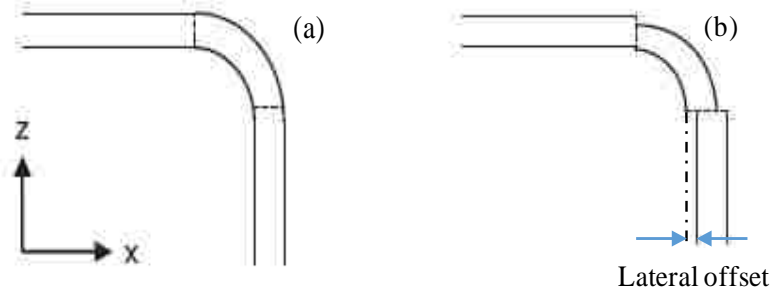


Figure 3-7. Comparison of waveguide bending, (a) is top view of bending without lateral offset; (b) is top view of bending with lateral offset [4].

Numerical investigation could identify optimum structure with the lowest radiation loss and modal mismatch loss. Note that the two main loss sources of bending are attributed to mode shift. Figure 3-8 represents that the optical mode shifts to outer edge of bent waveguide with various bend radius. The SOI ridge waveguide in our simulation has width of  $4\mu m$  and height of  $4.5\mu m$ , with silicon core and silicon-dioxide cladding layer. All the simulation results are at wavelength of  $1.31\mu m$ . Because the transverse mode is confined in x-y plane, the waveguide bending mostly affects the TE mode. Thus our simulation mainly focuses on fundamental TE mode along x direction.

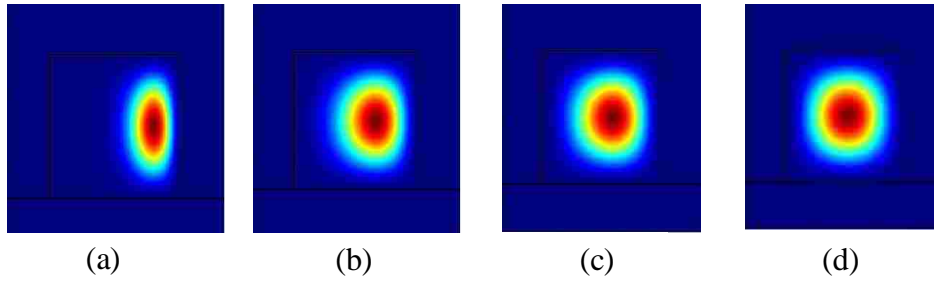


Figure 3-8.  $E_x$  component of fundamental TE mode for silicon ridge waveguide having height of  $4.5 \mu\text{m}$ , and width of  $4 \mu\text{m}$  for different bent radius. (a) Radius =  $100 \mu\text{m}$ , (b) Radius =  $500 \mu\text{m}$ , (c) Radius =  $1000 \mu\text{m}$ , (d) Radius =  $5000 \mu\text{m}$ .

Figure 3-8 shows that mode in bent waveguide tends to have smaller lateral shift when bending radius is bigger. Such results are also revealed as showed in Figure 3-6. However, larger bending radius results in the waste of space in the PIC board. Thus, low radiation loss with relatively small radius is needed. According to the numerical results of Figure 3-6, we choose bending radius of  $2000\mu\text{m}$  as the value to minimize radiation loss in waveguide bending. Figure 3-9 shows the waveguide bending loss as function of lateral offset in a bending waveguide with  $2000\mu\text{m}$  bending radius. The minimum total loss of  $0.025 \text{ dB}$  can be achieved when lateral offset reaches  $0.12\mu\text{m}$ .

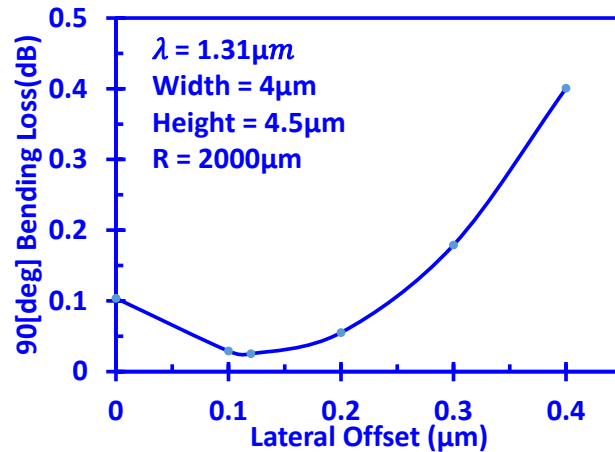


Figure 3-9. Bending loss of waveguide as a function of lateral offset ( $\mu\text{m}$ ) with lowest loss at lateral offset= $0.12 \mu\text{m}$ .

### 3.4. Tapered waveguide design and simulation results

Tapered waveguide is an indispensable optical component for connecting two waveguides with different dimensions. To achieve smooth surface for high coupling efficiency in the tapered waveguide, it requires one-die-at-a-time. Due to imperfection fabrication process of conventional CMOS structure, SOI tapered waveguide can only change size in one dimension. Figure 3-10 (a) shows the tapered waveguide in Lumerical FDTD Solutions, where red portion is silicon, and gray portion is silicon-dioxide substrate. The tapered waveguide structure connects two waveguides with same height and different width. In section 2.3, we reviewed the analytical model of a linearly tapered waveguide, where the analytical result shows oscillation when transmittance approaches unity. However, the analysis in chapter 2 is not perfect because the multiple reflection in tapered waveguide is not taken into account. In this section, we use FDTD simulation to precisely tracking the propagation of light in the tapered waveguide structure. Further optimization of tapered waveguide design for higher transmittance is necessary for low-loss interferometer in OCT system.

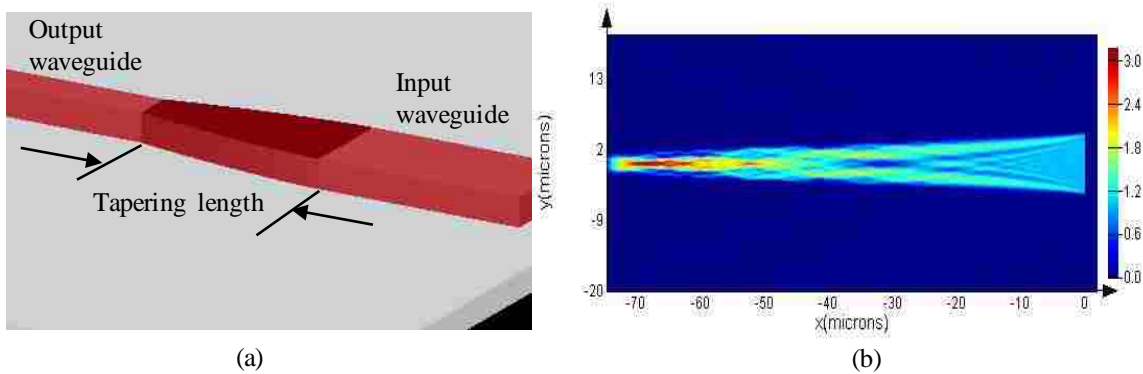


Figure 3-10. (a) tapered waveguide structure connecting with two waveguides with different width, red portion represents for silicon waveguide, and gray portion is silicon-dioxide substrate. (b) FDTD simulation results for a linearly tapered waveguide, where tapering length is  $66 \mu\text{m}$ , input waveguide width is  $9.5 \mu\text{m}$ , and output waveguide width is  $4 \mu\text{m}$ . Fundamental mode is initiated inside input waveguide.



Figure 3-10 (b) shows FDTD simulation result of a linearly tapered waveguide, where the light is guided into tapering section from input waveguide. The width of the tapering section decreases from 9.5 to 4  $\mu\text{m}$ , while the waveguide width is fixed at 4.5  $\mu\text{m}$ . From the top view of the FDTD simulation, diffraction from sidewalls of the linearly tapered waveguide is still visible. In this case the transmittance of such structure is 0.978. In order to achieve higher transmission with smaller dimension of tapered waveguide, improvement of tapering section is crucial.

Various approaches for enhancing transmittance of tapered waveguide structure has been proposed by literatures. Minhao Pu proposed extremely long ridge tapered waveguide for ultra-low-loss [17], Fenner Milton converted linearly tapered waveguide to parabolic-shape [18], others work on complex tapered waveguide structure [19]. Among all the proposed methods, the tapered waveguides proposed by Yunfei Fu [20] shows great improvement on transmission value. In that case, various shapes of taper structure are simulated for comparing in this section.

In order to study different shapes of tapered waveguide, we synthesis the shape model for describing all shapes we want to simulate. For linear taper, the shape function can be expressed as equation (3-4), in which the width of tapered waveguide changes along x axis. The  $a_0$  is half width of input waveguide section, and  $a_1$  is half width of output waveguide section. L is tapering length.

$$a(x) = a_0 + (a_1 - a_0) \frac{x}{L} \quad (3-4)$$

Similarly, the parabolic shape function can be represented as:

$$a(x) = a_0 + (a_1 - a_0) \left(\frac{x}{L}\right)^2 \quad (3-5)$$

Sinusoidal shape function is:

$$a(x) = \frac{a_1+a_0}{2} + \frac{a_1-a_0}{2} \cos\pi \frac{x}{L} \quad (3-6)$$

To generalize shape functions, tapering shape can be changed arbitrarily with function:

$$a(x) = a_0 + (a_1 - a_0)\left(\frac{x}{L}\right)^m \quad (3-7)$$

With equation (3-7), any tapering shape can be represented, where the taper's shape depends on the value of  $m$ . In order to find out the best shape of taper for higher transmission, we sweep the shape parameter  $m$ . Figure 3-11 shows the transmission versus tapering shape parameter  $m$ , where the waveguide height is  $4.5\mu m$ , input waveguide width is  $9.5\mu m$ , output waveguide width is  $4\mu m$ , taper length is  $60\mu m$ , and wavelength is  $\lambda = 1.31\mu m$ . As  $m$  varies from 1 to 2.5, transmission of tapered waveguide reaches peak of 0.9825 out of normalized input power at  $m=1.5$ . Choose tapering shape  $m=1.5$ , we can get very low coupling loss with short tapering length. Comparing results between linear tapered waveguide and the best tapering shape ( $m=1.5$ ), Figure 3-12 shows transmission of tapered waveguide under the same structure condition with  $\lambda = 1.31\mu m$ . Our results have a good agreement with the analytical results shown in chapter 2, where the transmission losses of tapered waveguide decrease when tapering length increases. According to Figure 3-12, tapered waveguide with shape factor  $m=1.5$  reaches lower-loss at shorter tapering length than linear taper ( $m=1$ ), and the average transmission loss is smaller. For example, at tapering length  $L=50\mu m$ , transmission loss for  $m=1.5$  is 0.09 dB comparing 0.12 dB for  $m=1$ . Our simulation shows that the shape of tapered waveguide is an essential role in transmission efficiency.

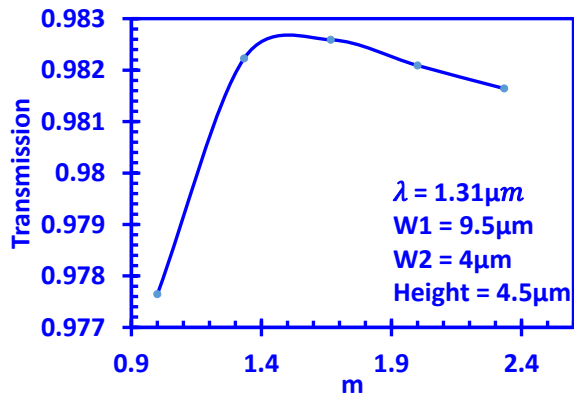


Figure 3-11. Simulation results show power transmission in tapered waveguide as function of tapering shape parameter  $m$ . the tapered waveguide connects two waveguides, where the input waveguide width is  $9.5 \mu m$ , output waveguide width is  $4 \mu m$ , waveguide height is  $4.5 \mu m$ , tapering length is  $60 \mu m$ , and operating wavelength is  $\lambda = 1.31 \mu m$ .

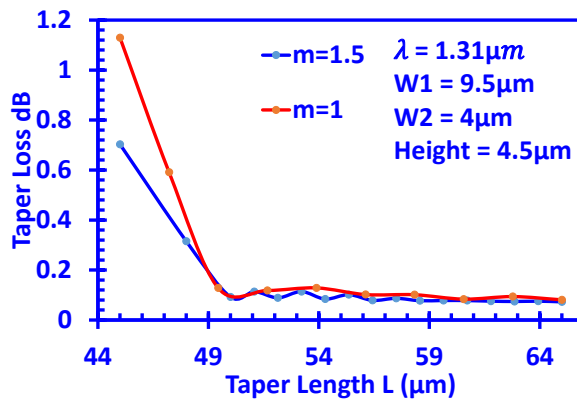


Figure 3-12. Simulation results of taper loss versus tapering length  $L$  at taper shape parameter  $m=1.5$  comparing with  $m=1$ (linear tapering).

### 3.5. Coupler simulation

Waveguide coupler is one of the fundamental elements in photonic integrated circuits (PIC). Physically, light propagates inside the waveguide based on critical angle and total internal reflection. The mode field confined inside waveguide is called guided mode. Oppositely, the evanescent mode of light exponentially decays outside of waveguide, which is the most important element for coupling. When two waveguides are close to one another, evanescent field of one waveguide overlaps with the mode of the other waveguide. Then the optical power transfers

between each other back and forth. The coupling coefficient is very sensitive to waveguide dimension, distance between two guides, and the coupling length. With two identical waveguides, we are able to design a fully coupled coupler with sufficient coupling length, which is capable of choosing desired polarization (TE and TM modes). Figure 3-13 shows the top and cross-sectional view of directional coupler, where the space between two silicon waveguides is denoted as  $s$ , and coupling length is denoted as  $L_{couple}$ .

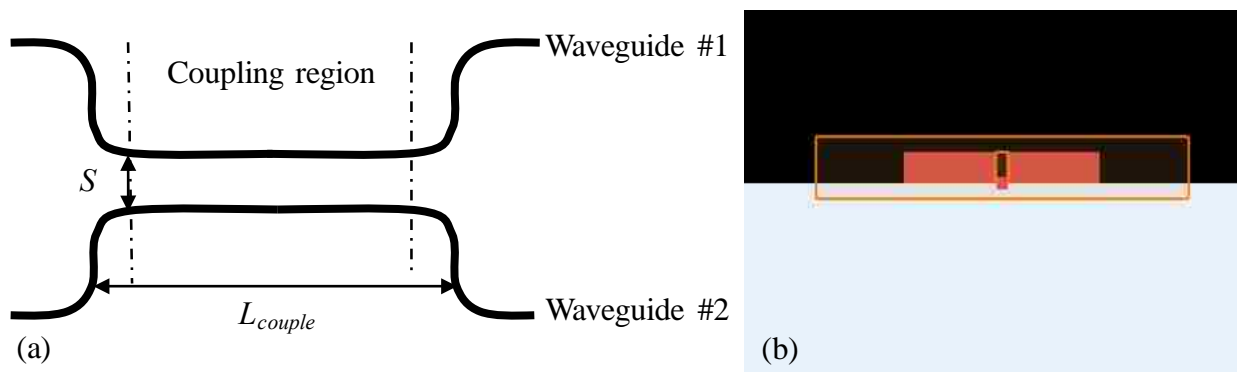


Figure 3-13. (a) Schematic of waveguide coupler, where the bending section determine the proximity between two waveguides. (b) Coupler cross-section in Lumerical FDTD solutions, where silicon waveguides are placed on top of silicon-dioxide substrate with air gap between two waveguides.

In chapter 2, we have reviewed the directional coupler with coupled mode theory [21] by accurately describing the feature of coupling coefficient as function of coupler parameters. However, due to the complexity of coupled-mode-theory, we only consider  $TE_0$  mode with 2-D coupler structure. In order to obtain more accurate result for 3-D coupler, we aim to design one proper coupler and analyze the coupling strength for fundamental  $TE_{10}$  mode. A simple approach, i.e. effective index method [22], could be applied to calculate coupling length. The field for both waveguides can be calculated by FDTD simulation.

By solving Maxwell equations in Lumerical FDTD Solution for a settled waveguide coupler, eigen mode solutions would define the corresponding effective index. For symmetric

directional coupler (waveguides are identical), coupling length for complete power transferring from one waveguide to the other satisfies equation (3-8) [23], where  $\lambda$  is wavelength,  $\Delta n$  is refractive index difference between evanescent mode and guided eigen mode. Characteristic of symmetric directional coupler coupling with different polarization (TE and TM mode) can easily be calculated with the coupling length function (3-9) [23], in which  $P_0$  is the total input power in the coupler, and  $P_2$  is the output power from waveguide #2.

$$P_2(L) = P_0 \sin^2\left(\frac{\pi L \Delta n}{\lambda}\right) \quad (3-8)$$

$$L = \frac{\lambda}{\pi \Delta n} \sin^{-1}\left(\sqrt{\frac{P_2}{P_0}}\right) \quad (3-9)$$

Setting silicon waveguide with  $4\mu m$  width and  $4.5\mu m$  height, and wavelength  $\lambda = 1.31\mu m$ , multiple modes would be generated inside two waveguides. Due to strong optical confinement of silicon and comparably large waveguide dimension, coupling strength would be strongly sensitive to coupler spacing  $s$ . By choosing spacing  $s$  in nanometer magnitude, coupling length  $L_c$  will explode to over 1000 times wavelength in millimeter scale.

Figure 3-14 shows symmetric directional coupler with proposed waveguide structure with spacing=2nm. The coupling  $TE_{10}$  with evanescent mode is showed in Figure 3-14 (b), Figure 3-14 (c) gives a closer view of coupler spacing where evanescent field can be identified clearly. Compare with eigen mode in Figure 3-15 the electrical field intensity is drawn with white line, and effective index is showed with color map. When the waveguides spacing is 2nm, the coupling length  $L_c$  for full power coupling is 2.330961mm for  $TE_{10}$  mode. Figure 3-16 shows the coupling between two waveguides along  $z$  direction, where waveguide structure has width of 500nm and height of 200nm. The spacing between two waveguides is set to  $s=2nm$ .

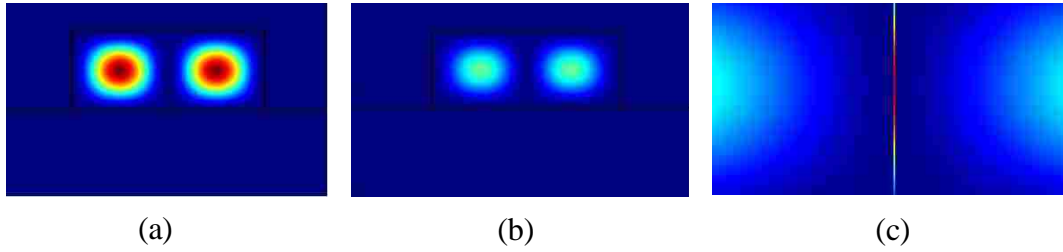


Figure 3-14. FDTD simulation for  $TE_{10}$  mode with  $h=4.5\mu m$ ,  $w=4\mu m$ ,  $\lambda = 1.31\mu m$ . Figure (a) shows the guided mode; figure (b) shows the evanescent mode; figure (c) shows a clearer view of evanescent field in between two waveguides.

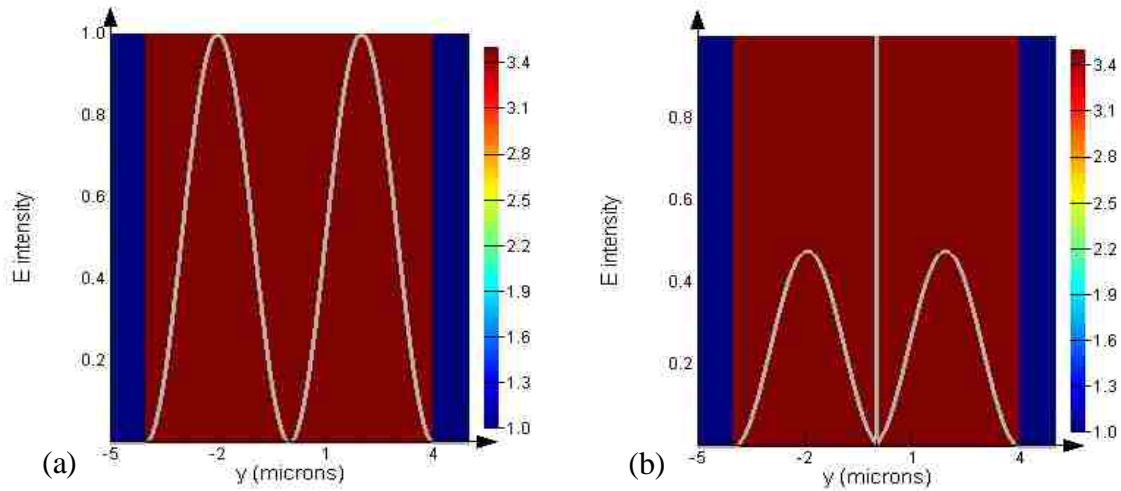


Figure 3-15. Eigen mode in symmetric directional coupler: (a) shows the guided mode and (b) shows the evanescent mode.

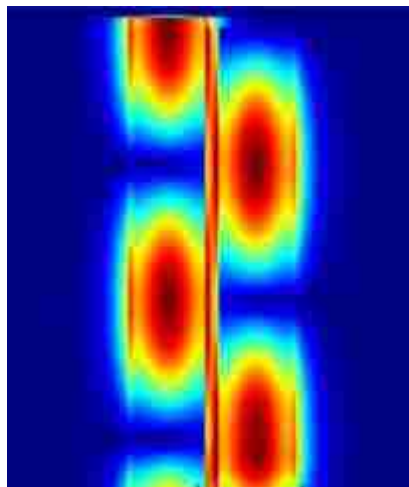


Figure 3-16. Power coupling between two waveguides back and forth, where coupler structure is  $w=0.5\mu m$ ,  $h=0.2\mu m$ ,  $s=50\text{ nm}$ , and  $\lambda = 1.55\mu m$ . Coupling length for this coupler structure is  $12.887\mu m$  [23].

Figure 3-17 shows coupling length as a function of coupler spacing with fundamental mode, where waveguides have  $h=4.5\mu m$ ,  $w=4\mu m$ ,  $\lambda = 1.31\mu m$ . The coupling length calculated in Figure 3-17 is for 50/50 directional coupler, where optical power from one waveguide will only transfer half of the power into the other waveguide. In that case, after specific coupling length, both waveguides of the 50/50 directional coupler will keep half of the initial input power. The coupling length can be calculated with  $P_0 = 1$ ,  $P_2 = 0.5$  and  $L = \frac{\lambda}{\pi\Delta n} \sin^{-1} \left( \sqrt{\frac{P_2}{P_0}} \right) = \frac{\lambda}{4\Delta n}$ . The trend of coupling length shows good agreement with analytical results from chapter 2, which is exponentially increasing as coupler spacing growing. On the other hand, for waveguide coupler in practical, the main loss comes from sidewall roughness propagation loss and insertion loss when the waveguide bends connect before and after the coupling region. Having simulation results from earlier sections, the scattering loss and bends loss can simply accumulate for power loss in symmetric silicon-on-insulator (SOI) 50/50 directional coupler.

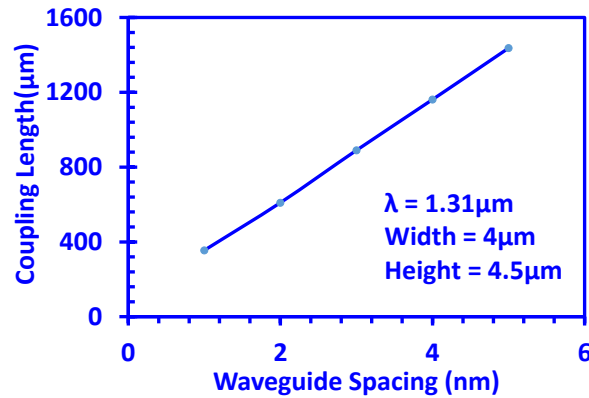


Figure 3-17. Coupling length versus coupler spacing for SOI ridge 50/50 directional coupler with fundamental mode, the waveguides have height of  $h=4.5\mu m$ , width of  $w=4\mu m$ , and the operating wavelength is  $\lambda=1.31\mu m$ .

### 3.6. Waveguide intersection analysis

Waveguide intersection is widely used for SOI chip design in order to obtain high-density and high-volume photonic systems. Whilst, low-crosstalk and low transmission loss is the main

desire for low-loss waveguide intersection design. Figure 3-18 (a) shows the schematic of waveguide intersection. Intersection crosstalk occurs when the optical wave from first waveguide interferes with the optical wave from the other waveguide in the crossing region, which couples light power between two waveguides. Crosstalk is relatively small when intersecting angle is large. Such trend has been presented in section 2.5. To suppress the crosstalk between two waveguides, perpendicular intersection can be further optimized to minimize crosstalk. On the other hand, transmission loss is induced by diffraction of optical field at the unbounded crossing region. In the crossing region, light wave expands freely without waveguide confinement, and the entire expanded mode can no longer be recovered after passing through the crossing region. Part of the light radiates away, and thus transmission loss occurs. With perpendicular intersection combined by straight waveguides, transmission loss is reported to be about 1.4 dB per crossing [24, 25]. In this section, we will mainly focus on the analysis of low-transmission-loss perpendicular waveguide.

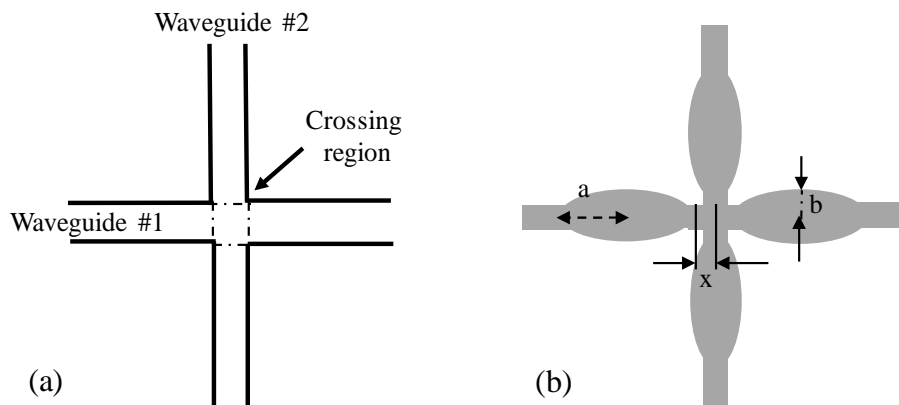


Figure 3-18. Schematic of waveguide intersection. Figure (a) is the schematic of directional intersecting waveguide with crossing region being defined. Figure (b) represents the structure of low-loss and low-crosstalk waveguide intersection we proposed, ellipse at each arm of intersection have long radius  $a$  and short radius  $b$ ,  $x$  is offset between ellipse and center point of crossing region.



Achieving the low-loss perpendicular waveguide has been widely studied and various intersection design has been proposed to suppressed transmission loss. One of the method is to minimize light diffraction in crossing region by adding tapered waveguide [26] or elliptical structures [25]. Further researches introduce material with lower index contrast in crossing region to minimize diffraction at the same time [27]. Other methods use optical resonance effect to couple light back into the right waveguide by creating resonant cavity in the structure [28]. With reference to these works, we propose an intersection structure by adding elliptical shape waveguide to the straight sections. Physically, elliptical waveguides will efficiently confine optical modes before the light passes through the crossing region. Figure 3-18 (b) shows the schematic structure we proposed with elliptical shape waveguide in each arm. Note that the distance between the end of ellipses and center of crossing is denoted as offset  $x$ . The long and short radius of the ellipse are represented by  $a$  and  $b$ .

The analysis of the proposed intersection structure was carried out by using FDTD simulation. Based on a ridge silicon-on-insulator (SOI) waveguide with height of  $4.5\mu m$ , width of  $4\mu m$ , at wavelength  $\lambda = 1.31\mu m$ , Figure 3-19 (a) and (b) show the FDTD simulation results with offset  $x=0$  and offset  $x=1.4\mu m$  respectively. Ellipses in the structure have long radius  $a=10\mu m$ , short radius  $b=4\mu m$ . Mode source is initiated at left arm of intersection, and passes through crossing region straightly to the other side. With no offset  $x$ , Figure 3-19 (a) shows very low crosstalk into perpendicular waveguide #2. The normalized optical power coupled into waveguide #2 is 0.00068 according the simulation results. However, optical diffraction cannot be eliminated with such structure, the transmission loss here is 0.256 dB. Figure 3-19 (b) shows the optical field with small lateral offset  $x$ , where the crosstalk is enlarged but diffraction goes smaller. The transmission loss with lateral offset  $x=0.8\mu m$  shrinks down to 0.142 dB. In order to compare

waveguide intersections with different ellipse shapes, Figure 3-19 (c) and (d) show the FDTD simulation results for  $a=9 \mu m$  and  $a=10.2 \mu m$  respectively. Short radius of these two structures is  $b=4 \mu m$ , and offset is  $x=0.7 \mu m$ . When ellipse long radius  $a=9 \mu m$ , crosstalk loss exists and diffraction is smaller than structure in Figure 3-19 (a). When ellipse long radius  $a=10.2 \mu m$ , crosstalk loss increase lightly, however transmission loss is much lower in crossing region. The transmission loss of Figure 3-19 (d) is 0.124dB. Because crosstalk loss is relatively smaller compared to transmission loss, we only consider transmission loss in this situation.

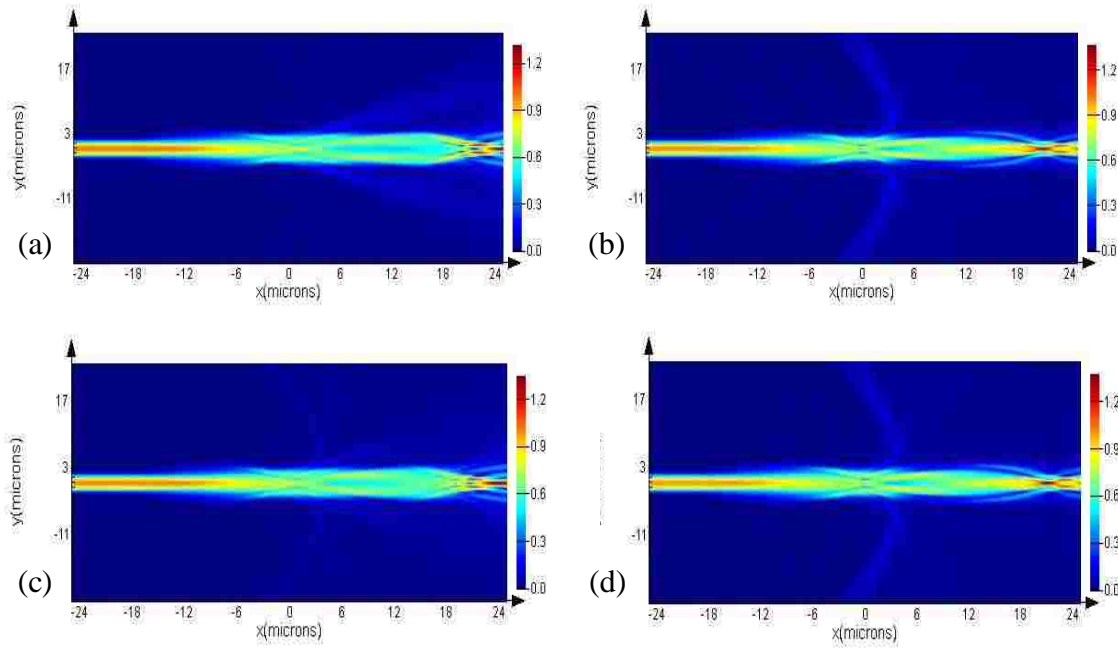


Figure 3-19. FDTD simulation picture of waveguide intersection with  $b=4 \mu m$ . Figure (a) shows proposed crossing with  $a=10 \mu m$ ,  $x=0 \mu m$ . Figure (b) shows proposed crossing with  $a=10 \mu m$ ,  $x=1.4 \mu m$ . Figure (c) shows proposed crossing with  $a=9 \mu m$ ,  $x=0.7 \mu m$ . figure (d) shows proposed crossing with  $a=10.2 \mu m$ ,  $x=0.7 \mu m$ .

In order to define the optimum lateral offset for minimizing transmission loss, Figure 3-19 (a) shows transmission loss as function of lateral offset  $x$  ( $\mu m$ ). The transmission loss approaches minimum value of 0.13 dB at  $x=0.7 \mu m$  with long radius  $a=10 \mu m$ , short radius  $b=4 \mu m$ ,  $\lambda =$

1.31 $\mu\text{m}$ . Figure 37 (b) shows the transmission loss with respect to the long radius  $a$ . As shown in this figure, transmission loss approaches minimum value of 0.124dB at  $a = 10.2 \mu\text{m}$  at short radius  $b=4 \mu\text{m}$ , and offset  $x=0.7 \mu\text{m}$ . According to the simulation results, the optimized low-loss perpendicular intersection waveguide with ellipse shape in each arm has  $a=10.2 \mu\text{m}$ ,  $b=4 \mu\text{m}$ ,  $x=0.7 \mu\text{m}$  with transmission loss of 0.124 dB/crossing.

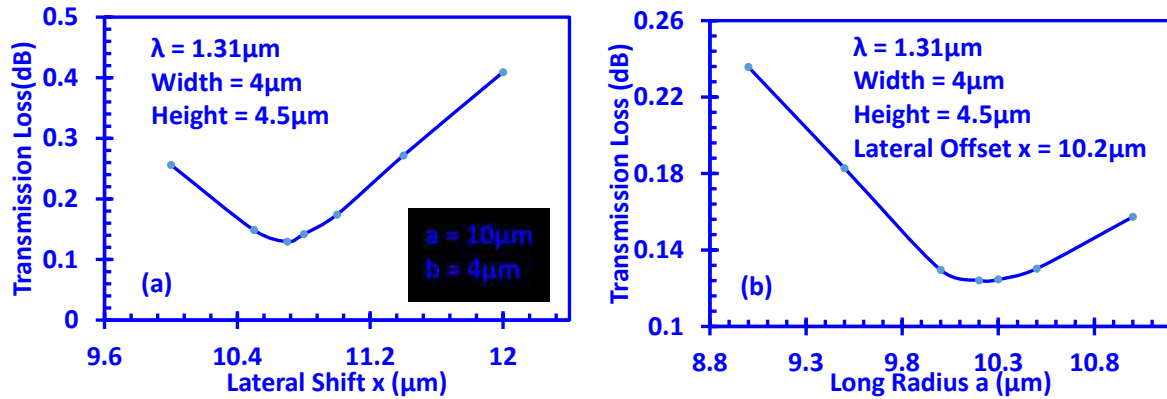


Figure 3-20. Simulation results of transmission loss as function of lateral shift and long radius. Figure (a) shows transmission loss versus lateral shift  $x$  for proposed intersection structure with  $a=10 \mu\text{m}$  and  $b=4 \mu\text{m}$ ; figure (b) shows transmission loss versus long radius  $a$ , simulated intersecting structure has  $b=4 \mu\text{m}$  and  $x=0.7 \mu\text{m}$ .

### 3.7. Total optimized loss for PIC-based OCT

Having designed and simulated optimized structure with FDTD method for each components of PIC system, we can define how much loss will be generated within the entire PIC. Figure 3-21 shows the PIC layout working as interferometer for OCT system. With SOI based PIC, scattering loss induced by sidewall roughness of the SOI waveguide is calculated. With roughness RMS  $\sigma = 13\text{nm}$ , and assuming the waveguides in PIC layout have height= $4.5 \mu\text{m}$  and width= $4 \mu\text{m}$ , the scattering loss is  $0.000124\text{dB}/\mu\text{m}$ . Additionally, the 90-degree SOI waveguide bending is designed to have bending radius  $r=2000 \mu\text{m}$  with  $0.12 \mu\text{m}$  lateral shift to straight waveguide section. Thus the minimum bending loss is achieved to  $0.025\text{dB}/\text{bending}$ . In the PIC layout we

have 54 bending totally. In that case, bending loss is a huge loss source for the system. Moreover, the tapered waveguide structure couples light from waveguide with width of  $9.5\ \mu\text{m}$  into PIC system. With tapered waveguide shape factor  $m=1.5$ , coupling loss is  $0.08\text{dB}$  with tapering length  $L=65\ \mu\text{m}$ . Furthermore, our simulation suggests that half power coupling length of a coupler is  $610\ \mu\text{m}$  with  $2\text{nm}$  spacing. Waveguide intersection is another big loss source for the PIC layout. In the optimized waveguide crossing structure we proposed, where each arm with ellipse shape of long radius  $a=10.2\ \mu\text{m}$ , short radius  $b=4\ \mu\text{m}$ , offset  $x=0.7\ \mu\text{m}$ , the transmission loss is  $0.124\ \text{dB/crossing}$ . Counting 12 intersections in the layout, total crossing loss would be  $1.488\text{dB}$ .

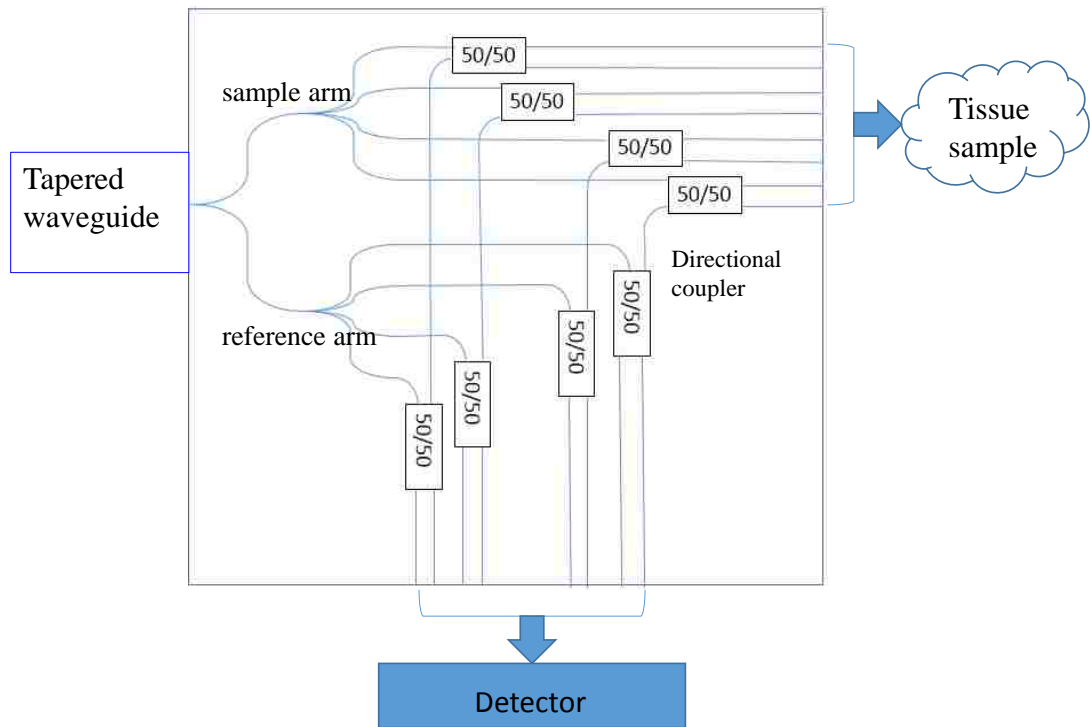


Figure 3-21. PIC layout with tapered waveguide [29].

As shown in Figure 3-21, optical light is coupled into PIC chip by tapered waveguide structure. Normalizing the input power to 1, the power coupled into the chip is  $98.16\%$ . Afterwards the light is split into the sample arm and reference arm with the same length of light path. Sample arm is to detect tissue sample and guide back the light reflected from tissue sample. Half of the

reflected power is dismissed through the 50/50 directional coupler second time. Afterwards, half of the reflected power passes through the intersection and combines with reference arm at 50/50 directional coupler. Taking into account all the bending loss, intersection loss, and surface roughness loss, 20% light power can be detected out of the PIC chip for final OCT data processing.

## References for chapter 3

1. Yee, K.S., *Numerical solution of initial boundary value problems involving Maxwell's equations in isotropic media*. IEEE Trans. Antennas Propag, 1966. **14**(3): p. 302-307.
2. Cela, *FDTD lecture*. 2014.
3. Lumerical, *solver finite difference time domain*.
4. Reed, G.T., *Silicon Photonics: the state of the art*. 2008: John Wiley & Sons.
5. Lee, K.K., et al., *Fabrication of ultralow-loss Si/SiO<sub>2</sub> waveguides by roughness reduction*. Optics letters, 2001. **26**(23): p. 1888-1890.
6. Dumon, P., et al., *Low-loss SOI photonic wires and ring resonators fabricated with deep UV lithography*. IEEE Photonics Technology Letters, 2004. **16**(5): p. 1328-1330.
7. Payne, F. and J. Lacey, *A theoretical analysis of scattering loss from planar optical waveguides*. Optical and Quantum Electronics, 1994. **26**(10): p. 977-986.
8. Marcuse, D., *Mode conversion caused by surface imperfections of a dielectric slab waveguide*. Bell System Technical Journal, 1969. **48**(10): p. 3187-3215.
9. Barwicz, T. and H.A. Haus, *Three-dimensional analysis of scattering losses due to sidewall roughness in microphotonic waveguides*. Journal of lightwave technology, 2005. **23**(9): p. 2719-2732.
10. Lee, K.K., et al., *Effect of size and roughness on light transmission in a Si/SiO<sub>2</sub> waveguide: Experiments and model*. Applied Physics Letters, 2000. **77**(11): p. 1617-1619.
11. Jaberansary, E., et al., *Scattering loss estimation using 2-D Fourier analysis and modeling of sidewall roughness on optical waveguides*. IEEE Photonics Journal, 2013. **5**(3): p. 6601010-6601010.
12. Lumerical. *PIC passive bent waveguide analysis*.
13. Marcatili, E., *Bends in optical dielectric guides*. Bell System Technical Journal, 1969. **48**(7): p. 2103-2132.
14. Qian, Y., et al., *Compact and low loss silicon-on-insulator rib waveguide 90 bend*. Optics express, 2006. **14**(13): p. 6020-6028.
15. Popovic, M., et al., *Air trenches for sharp silica waveguide bends*. Journal of lightwave technology, 2002. **20**(9): p. 1762.
16. Kitoh, T., et al., *Bending loss reduction in silica-based waveguides by using lateral offsets*. Journal of lightwave technology, 1995. **13**(4): p. 555-562.
17. Pu, M., et al., *Ultra-low-loss inverted taper coupler for silicon-on-insulator ridge waveguide*. Optics Communications, 2010. **283**(19): p. 3678-3682.
18. Milton, A.F. and W.K. Burns, *Mode coupling in optical waveguide horns*. IEEE Journal of Quantum Electronics, 1977. **13**: p. 828-835.
19. Dai, D., Y. Tang, and J.E. Bowers, *Mode conversion in tapered submicron silicon ridge optical waveguides*. Optics express, 2012. **20**(12): p. 13425-13439.
20. Fu, Y., et al., *Efficient adiabatic silicon-on-insulator waveguide taper*. Photonics Research, 2014. **2**(3): p. A41-A44.
21. Huang, W.-P., *Coupled-mode theory for optical waveguides: an overview*. JOSA A, 1994. **11**(3): p. 963-983.
22. Chiang, K.S., *Effective-index method for the analysis of optical waveguide couplers and arrays: an asymptotic theory*. Journal of lightwave technology, 1991. **9**(1): p. 62-72.
23. Lumerical, *PIC passive waveguide couplers evanescent*.

24. Chen, H. and A.W. Poon, *Low-loss multimode-interference-based crossings for silicon wire waveguides*. IEEE photonics technology letters, 2006. **18**(21): p. 2260-2262.
25. Fukazawa, T., et al., *Low loss intersection of Si photonic wire waveguides*. Japanese Journal of Applied Physics, 2004. **43**(2R): p. 646.
26. Little, B.E., *Low loss lateral optical waveguide intersections*, 2009, Google Patents.
27. Bogaerts, W., et al., *Low-loss, low-cross-talk crossings for silicon-on-insulator nanophotonic waveguides*. Optics letters, 2007. **32**(19): p. 2801-2803.
28. Johnson, S.G., et al., *Elimination of cross talk in waveguide intersections*. Optics Letters, 1998. **23**(23): p. 1855-1857.
29. Y.Y. Huang, W.S., L.Y. Yan, A.Nitkowski, A. Weinroth, N. Tansu, and C. Zhou, *Integrated Photonic Devices for Ultrahigh-Speed, Space-Division Multiplexing Optical Coherence Tomography*. 2016.

## 4. Summary and future direction

### 4.1. Conclusion

The main topic of this thesis is to design and analyze a low-loss photonic-integrated-circuits (PICs) chip as interferometer in high-performance optical coherence tomography (OCT) system for 3-D medical disease diagnose. Instead of using free space optical components, PIC chip brings stronger stability and smaller dimension for OCT system. Based on silicon-on-insulator (SOI) waveguide, the PIC can be easily fabricated due to the mature CMOS manufacturing industry. In order to calculate the total loss of the PIC chip, each loss source of the proposed PIC layout is introduced and simulated for the optimal structure.

We reviewed all loss sources with analytical model in chapter 2. The design and simulation of 3-D waveguide structure was carried out in chapter 3 by finite-difference-time-domain (FDTD) method for precise loss analysis. The calculated results obtained in chapter 3 match well with the analytical prediction in chapter 2. Surface roughness loss induced by SOI sidewall roughness is calculated in both chapters, where operating wavelength and roughness index are the key factors affecting surface roughness loss. Waveguide bending has been reviewed in chapter 2, and then simulated precisely in chapter 3 with specific bending radius and optimized lateral shift for low-loss design. Tapered waveguide couples light into one waveguide from a waveguide with different dimension. Our analysis in chapter 3 proposed an optimized shape of tapered waveguide for low-loss design through FDTD simulation. Couple-mode-theory is used for both coupler structure and intersection crosstalk in chapter 2. Chapter 3 precisely represents the loss in coupler and intersection with FDTD method. We also have further proposed a low-loss waveguide intersection section structure with ellipse at each arm of intersecting in chapter 3. Taking into account all loss



sources, the total loss for the proposed PIC chip is 7dB meaning that the output power is 20% of the initial input power.

In order to enhance power efficiency of PIC for high-quality OCT system, improving PIC layout design and reducing components loss is important. In our case, one of the major reason for large optical loss is the using of too many waveguide bendings in the PIC system, which dismiss over 50% of the input power. The other major cause for optical loss is that the 50/50 directional coupler will cause half power loss after guiding back the light reflected from tissue sample. The future direction of moving from table-top setup for OCT to on-chip OCT will be of great importance for the integrated health technologies.

# Curriculum Vitae

**Liangyue Yan**

**Cell Tel.:** 484-665-2613

**Email:** [liy414@lehigh.edu](mailto:liy414@lehigh.edu)

**Address:** 512 Taylor St., Bethlehem, PA, 18015, USA

**Birth day:** January 26<sup>th</sup>, 1992

**Research group:** <http://www.ece.lehigh.edu/~tansu/people.html>

## Education

---

**Lehigh University** **September, 2016 (Expected)**  
Master of Science in Electrical and Computer Eng.  
**Zhejiang Normal University**  
Bachelor of Science in Optical Information Science and Technology **June, 2014**

## Skill

---

Advanced Electrical Circuit Design, Photonics Systems and Integrated Circuits, Lumerical and R-Soft (FDTD), Matlab, Digital Circuit Design, VLSI Design, C programming

## Related Courses

---

Advanced Circuits and Systems, Semiconductor Lasers, Electromagnetisms, VLSI Design, Embedded System, Digital Circuits Design, Digital Control, Wireless Communication, and Semiconductor Devices

---

**Graduate Research Experience** **MS Research Assistant** **Lehigh University**  
**Period: June 2015 – present (till September 2016)**

**Conduct research work for MS thesis in Center for Photonics and Nanoelectronics at Lehigh University (Advisor: Prof. Nelson Tansu)**

- Nano/microphtonics for high extraction efficiency in GaN-based light-emitting diodes (LEDs)
  - Using microlens arrays and 2-D quasi-photonic crystal structures
  
- Miniaturizing the “table-top” optical coherence tomography (OCT) set up to chip-scale solutions
  - Integrated photonics structures for on-chip optical signal processing in OCT technology

---

**Undergraduate** **Zhejiang University**  
**Team Leader, Optical Communication Experiment Board** **07/2013-08/2013**

- Design and debug circuit, complete Protel diagram, and produce PCB board
- Programmed the microcontroller by C language for controlling LCD and speaker

**Team Leader, Inversion Algorithm of Concentration Distribution Based on TDLAS**  
**05/2013-12/2013**

- Develop a laser-based set up for detection of residual measurements in air, prototype development.

**Development of Optical Receivers in Fiber Optic Systems** **05/2012-12/2013**

- Development optical receiver board by using amplifier circuit chips LM353 and LM386
- Added encoder-decoder, replaced the analog signal with digital signal for signal transmission

**Technical Referred Publishes**

---

- **(Invited Conference Paper)** Y.Y. Huang, W.S., [L.Y. Yan](#), A.Nitkowski, A. Weinroth, N. Tansu, and C. Zhou, Integrated Photonic Devices for Ultrahigh-Speed, Space-Division Multiplexing Optical Coherence Tomography. 2016.

**Awards and Honors**

---

- |   |         |
|---|---------|
| ● Triple A Student  | 11/2013 |
| ● Third Scholarship for academic excellence in Zhejiang Normal University | 11/2013 |
| ● Excellent league member   | 05/2013 |

**Reference**

---

Prof. Nelson Tansu, Lehigh Univ – [tansu@lehigh.edu](mailto:tansu@lehigh.edu), Ph: 610-758-2678,  
[www.ece.lehigh.edu/~tansu](http://www.ece.lehigh.edu/~tansu)

Prof. Jon J. Wierer, Lehigh Univ – [jjw415@lehigh.edu](mailto:jjw415@lehigh.edu),  
[www.lehigh.edu/~cpn/people/faculty/wierer.html](http://www.lehigh.edu/~cpn/people/faculty/wierer.html)